

Elucidating the ^1H NMR relaxation mechanism in polydisperse polymers and bitumen using measurements, MD simulations, and models

Philip M. Singer,* Arjun Valiya Parambathu, Xinglin Wang,
Dilip Asthagiri, Walter G. Chapman, and George J. Hirasaki
*Department of Chemical and Biomolecular Engineering,
Rice University, 6100 Main St., Houston, TX 77005, USA*

Marc Fleury

IFP Energies Nouvelles, 1 Avenue de Bois-Prau, 92852 Reuil-Malmaison, France

The mechanism behind the ^1H NMR frequency dependence of T_1 and the viscosity dependence of T_2 for polydisperse polymers and bitumen remains elusive. We elucidate the matter through NMR relaxation measurements of polydisperse polymers over an extended range of frequencies ($f_0 = 0.01 \leftrightarrow 400$ MHz) and viscosities ($\eta = 385 \leftrightarrow 102,000$ cP) using T_1 and T_2 in static fields, T_1 field-cycling relaxometry, and $T_{1\rho}$ in the rotating frame. We account for the anomalous behavior of the log-mean relaxation times $T_{1LM} \propto f_0$ and $T_{2LM} \propto (\eta/T)^{-1/2}$ with a phenomenological model of ^1H - ^1H dipole-dipole relaxation which includes a distribution in molecular correlation times and internal motions of the non-rigid polymer branches. We show that the model also accounts for the anomalous T_{1LM} and T_{2LM} in previously reported bitumen measurements. We find that molecular dynamics (MD) simulations of the $T_1 \propto f_0$ dispersion and T_2 of similar polymers simulated over a range of viscosities ($\eta = 1 \leftrightarrow 1,000$ cP) are in good agreement with measurements and the model. The $T_1 \propto f_0$ dispersion at high viscosities agrees with previously reported MD simulations of heptane confined in a polymer matrix, which suggests a common NMR relaxation mechanism between viscous polydisperse fluids and fluids under confinement, without the need to invoke paramagnetism.

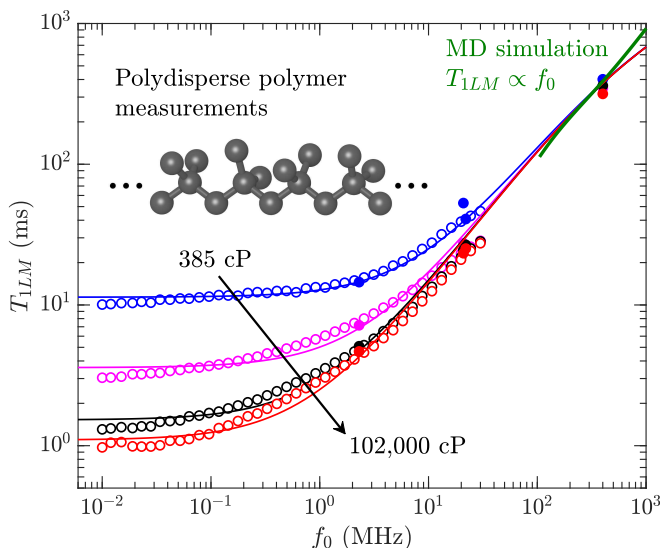


FIG. 1. Table of contents; graphical abstract.

I. INTRODUCTION

Among its many attributes, ^1H nuclear magnetic resonance (NMR) relaxation is a versatile non-destructive technique for measuring crude-oil viscosity and compo-

sition, thus providing a unique contribution to the characterization of light crude-oils, heavy crude-oils, and bitumen [1–45]. However, the ^1H NMR relaxation mechanism in crude oils at high viscosity such as heavy-oils and bitumen remains elusive and a topic of great debate.

One possible NMR relaxation mechanism in crude oils is surface paramagnetism [33, 35, 37, 38, 40], whereby the maltenes in the crude oils diffuse in and out of the asphaltene macro-aggregates, during which time they come into contact with the paramagnetic sites on the asphaltene surface. Another possible relaxation mechanism in crude oils is enhanced ^1H - ^1H dipole-dipole relaxation [1–5, 9, 13, 25, 30, 31, 43, 44], whereby the relaxation of the maltenes is enhanced by confinement from the transient nano-pores of the asphaltene macro-aggregates. Similarly, ^1H - ^1H dipole-dipole relaxation is also postulated to dominate for light hydrocarbons in the organic nano-pores of kerogen [46–53]. In fact, cross-linked asphaltene have been shown to be a good model for kerogen when modeling of the equilibrium partitioning of hydrocarbons in nanoporous kerogen particles [54].

In order to investigate the NMR relaxation mechanism in heavy-oils and bitumen, we previously reported a series of NMR measurements on polydisperse polymers and polymer-heptane mixes [42, 43]. Polymers are known to have similar rheology as heavy oils [55], making them good models for studying the rheology of viscous fluids. These polymers also have negligible amounts of paramagnetic impurities (< 100 ppm according to EPR), which makes them a good model for studying ^1H - ^1H dipole-dipole relaxation with measurements and molecular dynamics (MD) simulations. Many studies have been reported on the ^1H - ^1H dipole-dipole relaxation of monodis-

* ps41@rice.edu

perse polymers, including field-cycling relaxometry [56–58] and multiple-quantum techniques [59–62], from which a wealth of information about the molecular dynamics of monodisperse polymers is obtained. In our case, we use polydisperse polymers since bitumen and heavy-oils are highly polydisperse fluids. Furthermore, the polydisperse polymers are viscosity standards designed to have minimal shear-rate dependence on viscosity, which is important when comparing with NMR relaxation which is measured at zero shear-rate.

We previously showed that at high viscosities, the log-mean relaxation time T_{1LM} for the polydisperse polymers becomes independent of viscosity and proportional to frequency $T_{1LM} \propto f_0$ [42, 43]. This behavior presents significant deviations from the traditional Bloembergen, Purcell and Pound (BPP) model for ^1H - ^1H dipole-dipole relaxation of monodisperse hard-spheres [63] where $T_{1,BPP} \propto f_0^2 \eta / T$ is predicted at high viscosities. Furthermore for the polydisperse polymers, we find that the “plateau” value normalized to $f_0 = 2.3$ MHz, $T_{1LM} \times 2.3 / f_0 \simeq 3$ ms, is the *same* as previously reported bitumen data. This implies that the relaxation mechanism is independent of the paramagnetic concentration, and therefore that ^1H - ^1H dipole-dipole relaxation dominates over paramagnetism at high viscosities.

This then lead us to develop a phenomenological model based on ^1H - ^1H dipole-dipole relaxation which accounts for T_{1LM} plateau at high viscosities by lowering the frequency exponent in the BPP model [42, 43]. Lowering the frequency exponent implies a distribution in molecular correlation times of the viscous fluid, which is a similar approach to the phenomenological Cole-Davidson function [64, 65] commonly used for dielectric and NMR data of glycerol [66] and monodisperse polymers [58]. Our model also includes the presence of internal motions of the polymer branches through the Lipari-Szabo model [67, 68].

In this study, we further test our model on polydisperse polymers using T_1 field cycling relaxometry and $T_{1\rho}$ relaxation in the rotating frame. In the absence of paramagnetic impurities, we report on the anomalous viscosity dependence $T_{2LM} \propto (\eta/T)^{-1/2}$ for the polydisperse polymers at high viscosity, where a similar anomalous behavior was previously reported for bitumen [31, 44]. This again presents a significant departure from BPP where $T_{2,BPP} \propto (\eta/T)^{-1}$ is predicted at high viscosities. We report on MD simulations of T_1 and T_2 by ^1H - ^1H dipole-dipole relaxation of the polymer with viscosities in the range $\eta = 1 \leftrightarrow 1,000$ cP. The MD simulations show that $T_1 \propto f_0$ at high frequencies ($f_0 \gtrsim 100$ MHz), specifically $T_1 \times 2.3 / f_0 \simeq 3$ ms, in good agreement with measurements and our model at high viscosity. The MD simulations also confirm the dominance of *intra*-molecular over *inter*-molecular ^1H - ^1H relaxation at high viscosity, which was previously only assumed to be the case.

II. METHODOLOGY

A. Experimental

The polymers used in this study are listed in Table I. The average molecular weight M_w and poly-dispersivity index M_w/M_n were measured using gel permeation chromatography (GPC) using an Agilent Technologies 1200 module. The data in Table I indicate that the polymers are highly dispersive, up to $M_w/M_n \simeq 3.11$ in the case of B360000 poly(isobutene). The large polydispersivity of the polymers make them ideal for comparing with crude-oils, which are also highly dispersed as evidenced by their wide T_2 distributions [8]. In the case of the three poly(isobutene) polymers in Table I, the viscosity fit well to the functional form $\eta \simeq A M_w^\alpha$ [69], with $\alpha \simeq 2.4$ and $A \simeq 1.07 \times 10^{-4}$ in units of (cP) and (g/mol) at ambient [43]. An illustration of a section of poly(isobutene) is shown in Fig. 2, which was used for molecular dynamics (MD) simulations.

Name	Composition	η (25°C) (cP)	η (40°C) (cP)	M_w (g/mol)	M_w/M_n
B1060	Poly(1-decene)	1,040	385	4,204	1.49
B10200	Poly(isobutene)	10,700	4,060	2,256	2.13
B73000	Poly(isobutene)	68,100	28,700	4,368	2.53
B360000	Poly(isobutene)	333,000	102,000	9,436	3.11

TABLE I. Brand name, composition, viscosity η at 25°C and 40°C, average molecular weight M_w , and polydispersivity index M_w/M_n , for the Brookfield viscosity standards used in this study.

The viscosity measurements were made using a Brookfield AMETEK viscometer. The viscosities did not depend on shear-rate (within experimental uncertainties), thereby making them suitable viscosity “standards” for comparing with NMR measurements which are measured at zero shear-rate. The viscosity measurements were made at both ambient temperature ($\simeq 25$ °C) and at equilibrated temperatures of 40 °C using a circulation heat-bath. The viscosity data at 40 °C is used as a proxy for the NMR data at 38.4 °C.

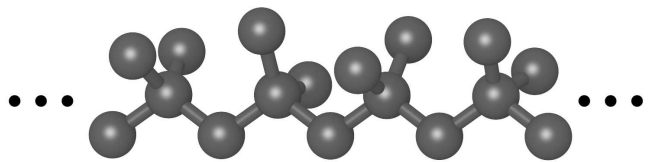


FIG. 2. Illustration of poly(isobutene), where only carbon atoms are shown for clarity. MD simulations of poly(isobutene) were performed with a 16-mer (i.e. 64 carbon atoms) with $M_w = 912$ g/mol and $\eta \simeq 1,000$ cP at ambient.

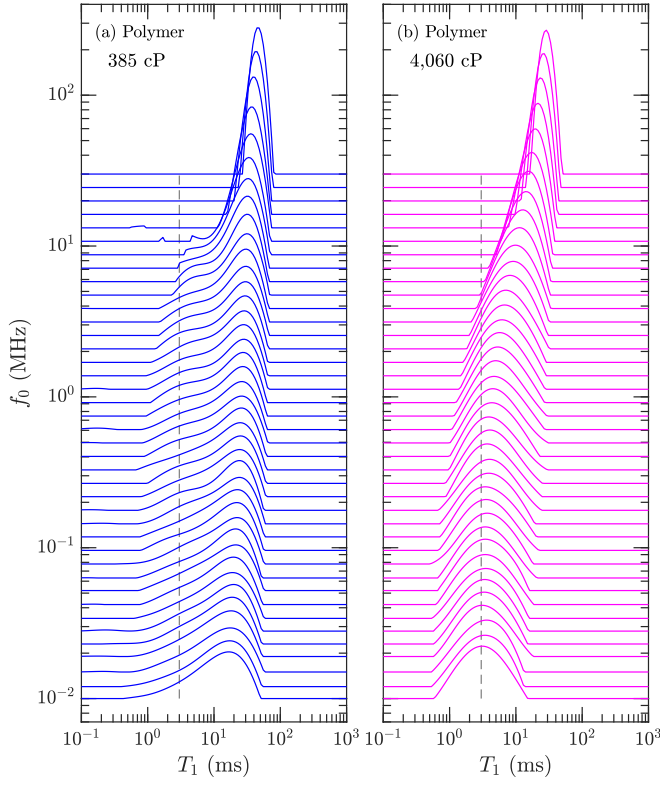


FIG. 3. T_1 distributions from field cycling (FC) relaxometry at 38.4°C for polymers listed in Table I. Dashed vertical line indicates FC ramp-time.

A 1 GHz electron paramagnetic resonance (EPR) apparatus was used to measure the concentration of paramagnetic ions *plus* the (weight equivalent) concentration of free radicals (i.e. unpaired valence electrons), which both contribute to NMR paramagnetic relaxation. The EPR data on the Brookfield viscosity standards indicated < 100 ppm paramagnetic impurities (i.e. the signal was below the detection limit of the apparatus). The paramagnetic concentration in the polymers is at least an order of magnitude less than the estimated $\simeq 1,000$ ppm for Athabasca bitumen [43, 70].

^1H NMR T_1 and T_2 measurements at a resonance frequency of $\omega_0/2\pi = f_0 = 2.3$ MHz were made with a GeoSpec2 from Oxford Instruments, with a 29 mm diameter probe. The samples were measured at ambient conditions ($\simeq 25^\circ\text{C}$) and after temperature equilibration to $\simeq 30^\circ\text{C}$. Additional measurements at $\simeq 35^\circ\text{C}$ were made by turning off the chiller and equilibrating to the magnet temperature. T_1 and T_2 measurements at $f_0 = 22$ MHz and $\simeq 30^\circ\text{C}$ were made with a special spectrometer from MR Cores at Core Laboratories, with a 30 mm diameter probe. T_1 and T_2 measurements at $f_0 = 400$ MHz at $\simeq 25^\circ\text{C}$ were made with a Bruker Avance spectrometer, in a 5 mm diameter probe.

^1H NMR T_1 , $T_{1\rho}$, and T_2 measurements at $f_0 = 21$ MHz and 38.4°C were made at IFP-EN on a Maran UI-

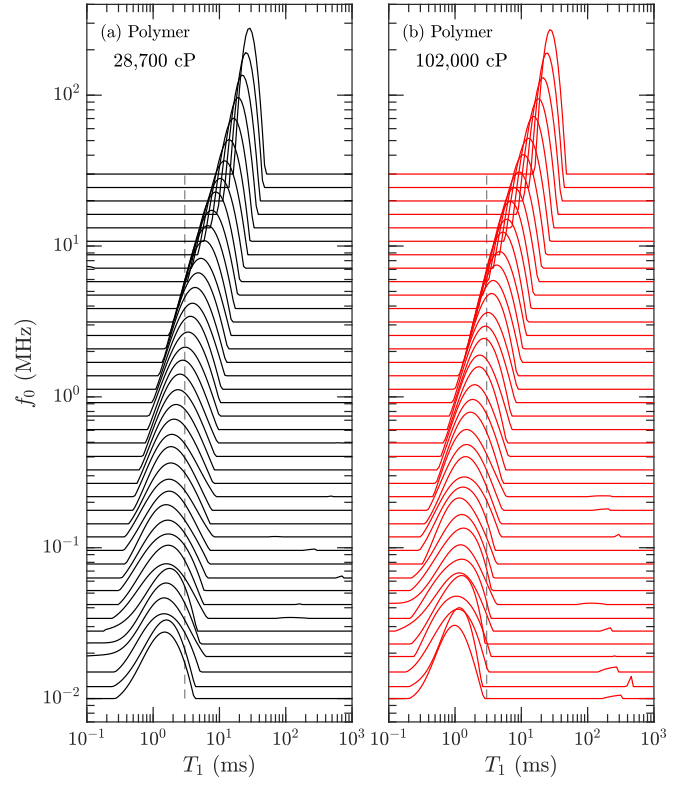


FIG. 4. T_1 distributions from field cycling (FC) relaxometry at 38.4°C for polymers listed in Table I. Dashed vertical line indicates FC ramp-time.

tra, with a 18 mm diameter probe. The $T_{1\rho}$ measurements in the rotating frame [71, 72] were made with a spin-locking frequency $\omega_1/2\pi = f_1 = 1.7$ kHz \leftrightarrow 42 kHz. Field cycling measurements were made on a Stellar fast field-cycling (FC) relaxometer from $f_0 = 0.01 \leftrightarrow 30$ MHz at 38.4°C, with a 10 mm diameter probe. All of the above T_2 measurements were measured using a CPMG sequence with echo spacings of $T_E = 0.1$ ms or less, except at $f_0 = 400$ MHz where T_2 was estimated from $T_2 \simeq 1/\pi\Delta f$, where Δf is the width of the NMR spectrum. The hydrogen index ($HI \simeq 1.17$) of the polymers is discussed in [43].

The T_1 , $T_{1\rho}$, and T_2 distributions of the pure polymers were determined using inverse Laplace transforms [73, 74]. The FC T_1 distributions shown in Figs. 3 and 4 tend to narrow with increasing frequency due to larger (absolute) longitudinal cross-relaxation [75, 76] (a.k.a. spin-diffusion). Figs. 3 and 4 also show the finite ramp-time of 3 ms required to ramp the field up and down. While in theory this does not effect the T_1 acquisition [77], it has been noted that it does effect broad T_1 distributions with fast relaxing components [78, 79]. Our relaxation model indicates that this is likely the case for the 102,000 cP polymer, where the log-mean T_{1LM} is most likely overestimated by a factor $\simeq 2^{1/2}$ at low frequencies.

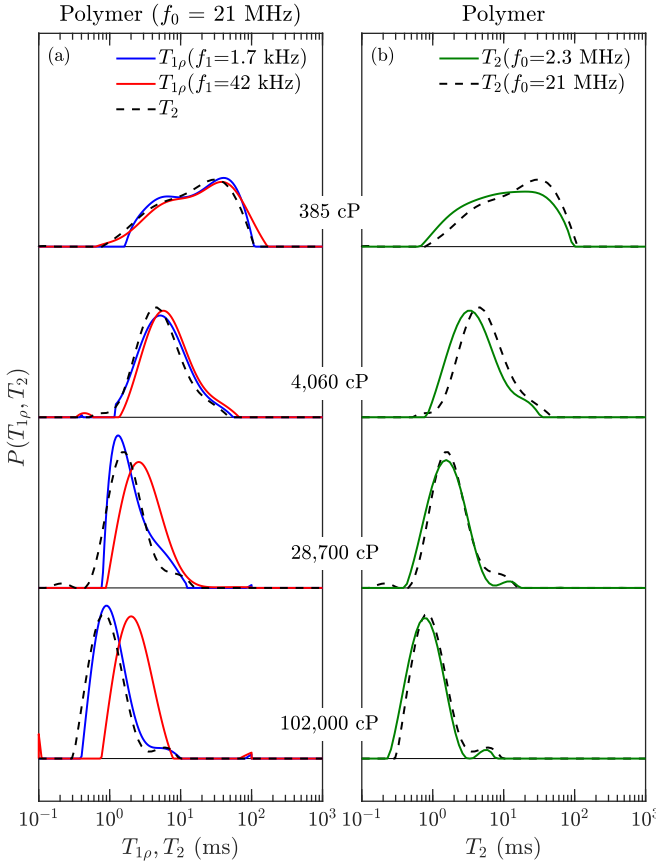


FIG. 5. (a) $T_{1\rho}$ distributions at $f_1 = 1.7$ kHz and $f_1 = 42$ kHz, along with T_2 distributions, all measured at $f_0 = 21$ MHz and 38.4°C . (b) T_2 distributions at $f_0 = 2.3$ MHz and 35°C , along with T_2 distributions at $f_0 = 21$ MHz and 38.4°C .

The $T_{1\rho}$ distributions at $f_1 = 1.7$ kHz and $f_1 = 42$ kHz are shown in Fig. 5, alongside the T_2 distribution. $T_{1\rho}$ and T_2 distributions tend to narrow with increasing viscosity, which is opposite to the trend in polydispersity index M_w/M_n in Table I. The narrowing may therefore be a result of larger transverse cross-relaxation (in the low frequency limit) with increasing viscosity (i.e. increasing correlation time) [76]. In the case of the most viscous polymer, Fig. 5 shows that $T_{1\rho}$ increases when going from $f_1 = 1.7$ kHz to 42 kHz, indicating the presence of molecular correlation times shorter than $\tau \lesssim (2\omega_1)^{-1} \simeq 1 \mu\text{s}$.

The log-mean values T_{1LM} , $T_{1\rho LM}$ and T_{2LM} of the distributions are used for data analysis and fitting to the model, where for example $T_{1LM} = \exp(\ln T_1)$, which is justified from the constituent viscosity model [8]. As shown in the Supporting Information, the effects of dissolved oxygen on T_1 as a function of frequency were measured for *n*-heptane, and the concentration of dissolved oxygen C_{O_2} in the polymer-heptane mix was predicted by MD simulations. The results indicate that the effects of dissolved oxygen on T_1 (and T_2) are negligible for all the polymers at all frequencies.

B. Relaxation model

The underlying expressions for T_1 , T_2 and $T_{1\rho}$ in an isotropic system are given by [80, 81]:

$$\begin{aligned} \frac{1}{T_1} &= J(\omega_0) + 4J(2\omega_0), \\ \frac{1}{T_2} &= \frac{3}{2}J(0) + \frac{5}{2}J(\omega_0) + J(2\omega_0), \\ \frac{1}{T_{1\rho}} &= \frac{3}{2}J(2\omega_1) + \frac{5}{2}J(\omega_0) + J(2\omega_0). \end{aligned} \quad (1)$$

$J(\omega_0)$ is the spectral density at the resonance frequency $\omega_0 = 2\pi f_0$. The expression for T_1 in the rotating frame, $T_{1\rho}$, is similar to T_2 except that the zero-frequency term $J(0)$ is replaced by $J(2\omega_1)$ where $\omega_1 = 2\pi f_1$ is the spin-locking frequency [71]. Note that Eq. 1 does not assume a model for the spectral density $J(\omega)$.

1. BPP model

The BPP model for the spectral-density $J_{\text{BPP}}(\omega)$ for intra-molecular ^1H - ^1H dipole-dipole relaxation is given by the following [63]:

$$J_{\text{BPP}}(\omega) = \frac{1}{3} \Delta\omega_R^2 \frac{2\tau_\eta}{1 + (\omega\tau_\eta)^2}, \quad (2)$$

$$\tau_\eta = \frac{4\pi}{3k_B} R^3 \frac{\eta}{T}, \quad (3)$$

$$\Delta\omega_R^2 = \frac{9}{20} \left(\frac{\mu_0}{4\pi} \right)^2 \hbar^2 \gamma^4 \frac{1}{N} \sum_{i \neq j} \frac{1}{r_{ij}^6}. \quad (4)$$

The BPP model assumes the Stokes-Einstein-Debye relation for hard spheres, where τ_η is the rotational correlation-time, η/T is viscosity over temperature, and R is the Stokes radius. The constant $\Delta\omega_R^2$ is the “second-moment” (i.e. the strength) of the intra-molecular ^1H - ^1H dipole-dipole interactions (where r_{ij} is the ^1H - ^1H distance between pairs i and j). Note that the BPP model is only valid in the motional-narrowing regime where $\Delta\omega_R\tau_\eta \ll 1$ [81], which is assumed to be the case throughout.

The BPP model introduces the important concept of the fast-motion (i.e. low viscosity) regime ($\omega_0\tau_\eta \ll 0.615$) where $T_1/T_2 = 1$:

$$T_{1,\text{BPP}} = T_{2,\text{BPP}} \propto \left(\frac{\eta}{T} \right)^{-1} \quad \text{for } \omega_0\tau_\eta \ll 0.615 \quad (5)$$

and the slow-motion (i.e. high viscosity) regime ($\omega_0\tau_\eta \gg 0.615$) where $T_1/T_2 > 1$:

$$T_{1,\text{BPP}} \propto f_0^2 \frac{\eta}{T} \quad \text{for } \omega_0\tau_\eta \gg 0.615 \quad (6)$$

$$T_{2,\text{BPP}} \propto \left(\frac{\eta}{T} \right)^{-1} \quad \text{for } \omega_0\tau_\eta \gg 0.615. \quad (7)$$

2. New relaxation model

The BPP model fails for polydisperse polymers and bitumen at high-viscosity. In particular, BPP predicts that $T_1 \propto f_0^2 \eta / T$ at high-viscosities, while measurements clearly indicate that $T_{1LM} \propto f_0$ is independent of viscosity. As such, a phenomenological model was developed where the frequency exponent in Eq. 2 is lowered from the BPP value $(\omega\tau)^2$ to $(\omega\tau)^1$. This has the effect of dropping τ_η (and therefore η/T) out of the equation in the slow-motion regime ($\omega_0\tau_\eta \gg 1$) [42, 43]. In the Supporting Information, we show that our model for the frequency exponent $(\omega\tau)^1$ is similar to the limiting case of the phenomenological Cole-Davidson function commonly used for dielectric data for glycerol [64, 65], as well as for NMR data of glycerol and monodisperse polymers [58].

The consequence of changing the frequency exponent is to introduce a distribution $P_R(\tau)$ in local rotational correlation times τ . This is justified by Woessner's theories which show that as the molecule becomes less spherical, the internal motions in the molecule become more complex, and the distribution in correlation times becomes more pronounced [82, 83]. We also note that according to Woessner's theories, simple fluids show a large distribution in correlation times when their motion is restricted by nano-confinement [84].

Besides changing the frequency exponent, our model also allows for the existence of internal motions of non-rigid polymers using the Lipari-Szabo (LS) model [67, 68]. Changing the frequency exponent to $(\omega\tau_\eta)^1$ in the BPP model and applying the LS model results in the following spectral density:

$$J_P(\omega) = \frac{1}{3} \Delta\omega_R^2 \left(S^2 \frac{2\tau_R}{1 + \omega\tau_R} + (1 - S^2) \frac{2\tau_L}{1 + \omega\tau_L} \right) \quad (8)$$

where the subscript P in $J_P(\omega)$ refers to the ‘‘Plateau’’, and $\tau_R \gg \tau_L$ is assumed. τ_R is defined as the slow rotational correlation-time of the whole polymer molecule, which depends on viscosity. The order parameter S^2 is a measure of the rigidity of the polymer molecule, where $S^2 = 1$ for completely rigid molecules with no internal motion of the polymer branches, and $S^2 = 0$ for completely non-rigid molecules with full internal motion of the polymer branches. τ_L is the local correlation-time, which characterizes the fast τ_L ($\simeq 10$'s ps) motions of the polymer branches.

Eq. 8 predicts the following expression in the slow-motion ($\omega\tau_R \gg 1$) regime:

$$J_P(\omega) \simeq \frac{1}{3} \Delta\omega_R^2 \left(S^2 \frac{2}{\omega} + (1 - S^2) 2\tau_L + \dots \right) \quad (9)$$

which leads to the following approximation for T_{1LM} :

$$\frac{1}{T_{1LM}} \simeq \frac{2\Delta\omega_R^2 S^2}{\omega_0} \left(1 + \frac{5}{3} \frac{1 - S^2}{S^2} \omega_0\tau_L + \dots \right). \quad (10)$$

In other words, the leading order term is $T_{1LM} \propto f_0$, which is independent of viscosity. A deviation from

linearity $T_{1LM} \propto f_0$ occurs at high frequencies when $\omega_0\tau_L \simeq 1$. This turns out to be more prominent for bitumen than for the polydisperse polymers, where τ_L is larger for bitumen (see below). We note that the temperature dependence of τ_L is most likely present but much less than the temperature dependence of τ_R (which depends on viscosity).

Eq. 8 also predicts the following approximation for T_{2LM} in the slow-motion regime:

$$\frac{1}{T_{2LM}} \simeq \frac{10}{3} \Delta\omega_R^2 S^2 \tau_R + \dots, \quad (11)$$

$$\text{where } \tau_R = (\tau_\eta\tau_0)^{1/2}.$$

The phenomenological relation $\tau_R = (\tau_\eta\tau_0)^{1/2}$ is introduced in [37, 44], which relates τ_R to the Stokes-Einstein-Debye correlation time $\tau_\eta \propto \eta/T$ (Eq. 3) at high viscosities. τ_0 is a constant, which leads to the prediction that $T_{2LM} \propto \tau_R^{-1} \propto (\eta/T)^{-1/2}$, in agreement with previously published bitumen data [31, 44] and the polydisperse polymer data shown below.

Two theories have been proposed for the relation $T_{2LM} \propto (\tau_\eta\tau_0)^{-1/2} \propto (\eta/T)^{-1/2}$ at high viscosity. The first theory by Korb *et al.* [37] stipulates that τ_0 (referred to as τ_{1D} in [37]) corresponds to a quasi-1D translational diffusion time of a maltene molecule within the transient nano-porous network of quasi immobile asphaltene macro-aggregates. $\tau_0 \propto \eta/T$ below a critical viscosity $\eta \ll \eta_c$ (with $\eta_c \simeq 300$ cP), while τ_0 is constant above the critical viscosity $\eta \gg \eta_c$. While [37] uses this theory in the context of paramagnetism, their model for τ_R can also apply here in the context of ^1H - ^1H dipole-dipole relaxation. The second theory [44] arrives at the same dependence of $T_{2LM} \propto (\tau_\eta\tau_0)^{-1/2} \propto (\eta/T)^{-1/2}$ at high viscosity, but τ_0 (referred to as τ_a in [44]) is dominated by the maltene's residence time τ_{res} in the asphaltene cluster (i.e. $\tau_0 \simeq \tau_{res}$), which is independent of viscosity.

Finally we note that the expression for T_{2LM} (Eq. 11) contains the factor $10/3$, implying that T_2 is in the fast-motion regime (i.e. independent of frequency) even when $\omega_0\tau_R \gg 1$. This is motivated by the interpretation of the polydisperse polymer and bitumen data presented below.

C. MD simulations

Molecular dynamics (MD) simulations of monodisperse polymers were conducted. Four different chain lengths of poly(isobutene) (see Fig. 2) were simulated at 25°C: a 16-mer, 8-mer, 4-mer and 2-mer. The viscosity of the 16-mer and 8-mer were estimated using the relation $\eta = A M_w^\alpha$ [69], with $\alpha \simeq 2.4$ and $A \simeq 1.07 \times 10^{-4}$ in units of (cP) and (g/mol) at ambient [43]. For example, in the case of the 16-mer where $M_w = 912$ g/mol, this predicts a viscosity of $\eta \simeq 1,000$ cP. The viscosities of the 4-mer and 2-mer were predicted using the empirical relation $T_{2LM} \simeq 9.56 (\eta/T)^{-1}$ [9] in units of (ms) and (cP/K).

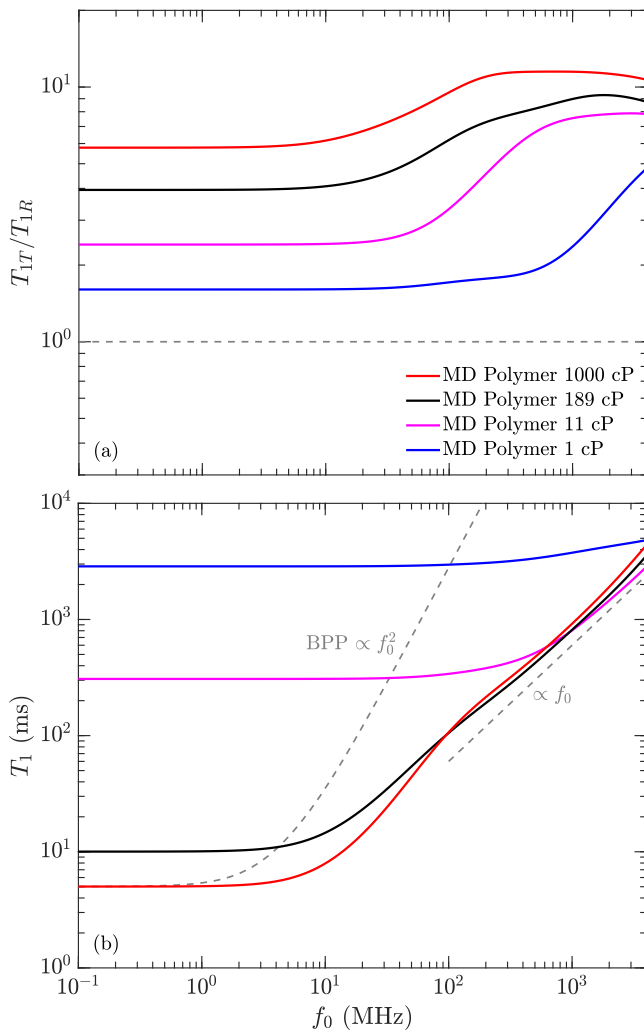


FIG. 6. (a) MD simulations of the ratio of inter-molecular to intra-molecular relaxation times T_{1T}/T_{1R} as a function of frequency for the four polymers. (b) Total relaxation time T_1 as a function of frequency for the four polymers. Also shown are the BPP prediction ($T_1 \propto f_0^2$), and the observed trend ($T_1 \propto f_0$) above $f_0 > 100$ MHz.

MD simulations of the intra-molecular ($T_{1R,2R}$) [63] and inter-molecular ($T_{1T,2T}$) [85, 86] ^1H - ^1H dipole-dipole relaxation were then computed for the polymers, from which the total relaxation times ($T_{1,2}$) are calculated:

$$\frac{1}{T_{1,2}} = \frac{1}{T_{1R,2R}} + \frac{1}{T_{1T,2T}}. \quad (12)$$

The procedure for the MD simulations are the same as reported elsewhere [87–89], and details are given in the Supporting Information.

Fig. 6(a) shows the ratio of inter-molecular to intra-molecular relaxation times T_{1T}/T_{1R} as a function of frequency for the four polymers. A value larger than unity $T_{1T}/T_{1R} > 1$ indicates that intra-molecular relaxation dominates, while $T_{1T}/T_{1R} < 1$ indicates that inter-

molecular relaxation dominates. We find that $T_{1T}/T_{1R} > 1$ increases with increasing viscosity, implying that intra-molecular relaxation dominates (by at least an order of magnitude) at high viscosities ($\eta \gtrsim 1,000$ cP). T_{2T}/T_{2R} (not shown) show similar results. These findings justify the assumption in our model (Eq. 8) that intra-molecular relaxation dominates over inter-molecular relaxation.

Fig 6(b) shows the total relaxation T_1 (Eq. 12) as a function of frequency for the four polymers. The lowest viscosity (1 cP) polymer shows high T_1 values and minimal dispersion (i.e. minimal frequency dependence). On the other hand, the highest viscosity polymers show significant dispersion. The 189 cP and 1,000 cP polymers merge above $f_0 > 100$ MHz into a linear relation $T_1 \propto f_0$. This behavior is exactly predicted by the model (Eq. 10), namely that $T_1 \propto f_0$ is independent of viscosity. The $f_0 > 100$ MHz region for the 1,000 cP polymer is compared with measurements and the model below.

We note that a similar relation was previously reported from MD simulations of heptane confined in a polymer matrix, where the surface relaxation T_{1S} of heptane followed $T_{1S} \propto f_0$ under confinement [53]. This implies a connection between the molecular dynamics of high-viscosity fluids and low-viscosity fluids under confinement.

III. RESULTS AND DISCUSSIONS

The results and interpretation are organized as follows. In section A we present the T_{1LM} data for polydisperse polymers and bitumen in the slow-motion (i.e. high-viscosity) regime, and we use Eq. 10 to extract the free parameters S^2 and τ_L (Table II). In section B we present the T_{2LM} data for polydisperse polymers and bitumen in the slow-motion (i.e. high-viscosity) regime, and we use Eq. 11 to extract the free parameter τ_0 (Table II). In section C we present the full frequency dependence of T_{1LM} and T_{2LM} data for the polydisperse polymers spanning both the fast- and slow-motion regimes, and we use the full expression Eq. 8 to extract τ_0 for each polymer (Table III).

A. T_{1LM} for polydisperse polymers and bitumen

The results for T_{1LM} for crude oils (including bitumen) and polydisperse polymers are shown in Fig. 7(a). The crude-oil data are taken from various sources listed in the legend. The most recent addition is the bitumen data at $f_0 = 400$ MHz by Kausik *et al.* [44], measured over a range of temperatures ($30^\circ\text{C} \leftrightarrow 90^\circ\text{C}$).

Also shown in Fig. 7(a) is the BPP prediction [63] at $f_0 = 2.3$ MHz and 400 MHz from Eq. 2. The crude oils roughly follow the BPP prediction $T_{1LM} \propto (\eta/T)^{-1}$ at low viscosities, however T_{1LM} clearly plateaus at high viscosity. Also shown are the MD simulations at 400 MHz

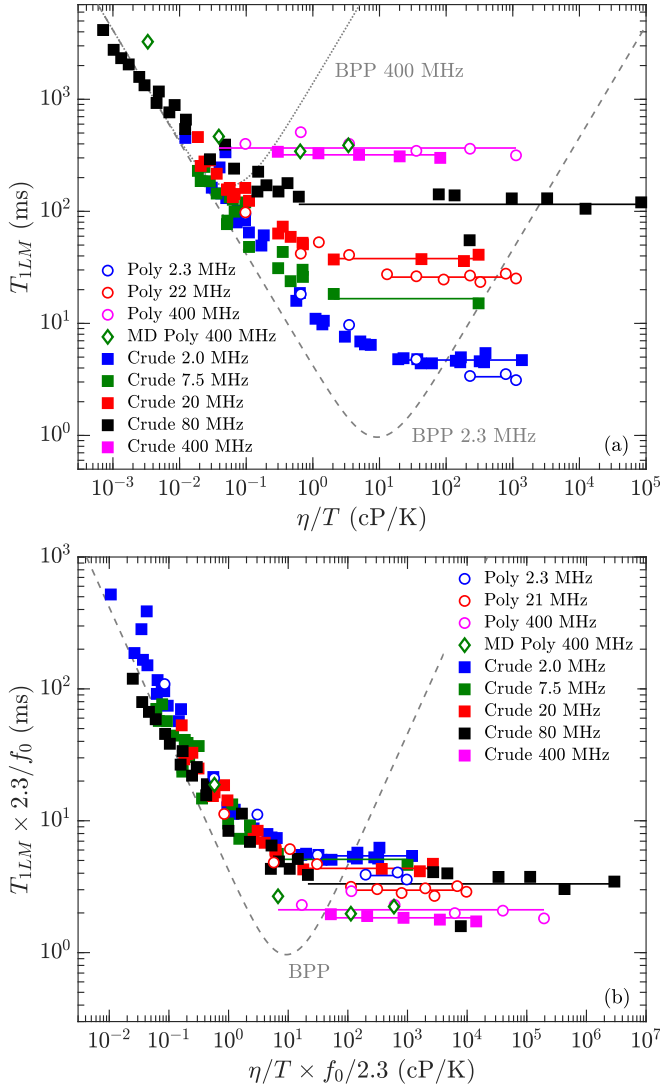


FIG. 7. (a) T_{1LM} vs. η/T for the polydisperse polymers in Table I at 2.3 MHz, 21 MHz, and 400 MHz, and MD simulations of the polymer poly(isobutene) in Fig. 2 at 400 MHz. Also shown are previously published crude-oil and bitumen data at 2.0 MHz (LaTorraca *et al.* [6], Yang *et al.* [25]), at 7.5 MHz and 20 MHz (Zhang *et al.* [10]), at 80 MHz (Vinegar *et al.* [2]), and at 400 MHz (Kausik *et al.* [44]). Horizontal lines at each frequency indicate log-average of T_{1LM} in slow-motion (i.e. high-viscosity) region. Curved lines are the BPP prediction [63] at 2.3 MHz and 400 MHz. (b) Same data as in (a), but plotted on frequency normalized axes (normalized to $f_0 = 2.3$ MHz).

for the polymers, which are consistent with the polydisperse polymer measurements.

Fig. 7(b) shows the same data as Fig. 7(a) but on a frequency normalized scale. More specifically, the x-axis (η/T) is multiplied by $f_0/2.3$ with f_0 in units of MHz, while the y-axis (T_{1LM}) is divided by $f_0/2.3$. Frequency normalizing has the effect of collapsing the frequency dependence of the BPP model onto one universal

curve [10]. It also has the effect of collapsing the bitumen and polymer data in the slow-motion regime onto one plateau value given by $T_{1LM} \times 2.3/f_0 \simeq 3$ ms, i.e. $T_{1LM} \propto f_0$. The more recent bitumen data at 400 MHz shows a slight departure from the low frequency data, namely the plateau value is lower than at lower frequencies. As shown below, the model takes this departure into account with the $\omega_0\tau_L$ term in Eq. 10.

Fig. 8 shows T_{1LM} data for the polydisperse polymers and the bitumen in the slow-motion regime (i.e. high-viscosity) regime, which corresponds to data within the horizontal lines (the log-average) in Fig. 7(a). The best fit to the new model using Eq. 9 and Eqs. 1 are shown for both polydisperse polymers and bitumen, and the best fit parameters are shown in Table II. The second moment is fixed to $\Delta\omega_R/2\pi = 20.0$ kHz, which is the value for *n*-heptane [43]. A Stokes radius of $R = 1.85$ Å is used for the polymers, which is the value needed to match the correlation $T_{1LM,2LM} = 9.56 (\eta/T)^{-1}$ in the low-viscosity regime [9]. A slightly larger Stokes radius of $R = 2.47$ Å is used, which is the value needed to match the correlation $T_{1LM,2LM} = 4.0 (\eta/T)^{-1}$ in the low-viscosity regime [8].

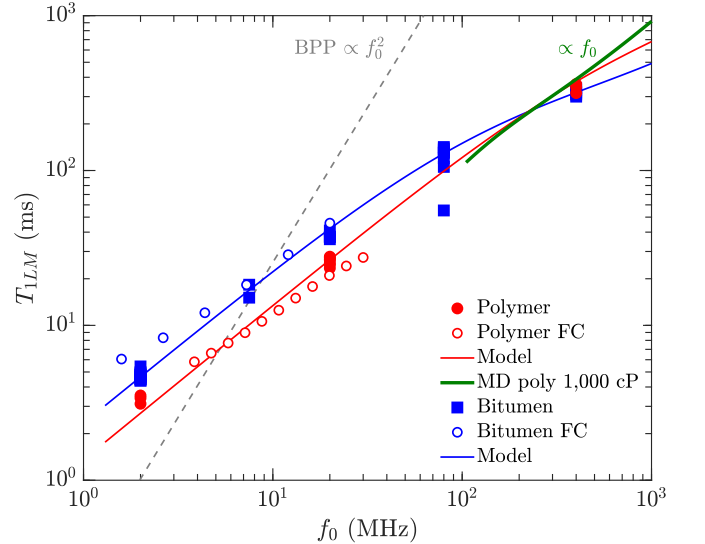


FIG. 8. T_{1LM} vs. f_0 data for polydisperse polymers and bitumen taken from Fig. 7(a), where only data from the slow-motion (i.e. high viscosity) regime are included. Bitumen data are taken from various sources (see Fig. 7 caption), while field cycling (FC) data for bitumen are taken from [44]. Also shown are FC data for the 102,000 cP polymer. Solid curves are fits using the model in Eq. 10 with fitting parameters shown in Table II. MD simulations of the 1,000 cP polymer are shown above $f_0 > 100$ MHz, corresponding viscosity independent region (see Fig. 6) where $T_1 \propto f_0$. BPP prediction $T_1 \propto f_0^2$ is also shown.

We note that the fact that $T_{1LM,2LM}$ are consistent with a constant Stokes radius R in the low-viscosity regime, i.e. R is independent of molecular size (and therefore viscosity), clearly shows that $T_{1,2}$ are probes of the

local molecular dynamics. This is in stark contrast to the radius of gyration R_g which depends on the molecular size [87].

The first free-parameter in the model is the order parameter S^2 , which characterizes the rigidity of the molecule. $S^2 \simeq 0.147$ is found for the polydisperse polymers, which is consistent with previously reported data for monodisperse polymers at high molecular-weights $M_w > 4,000$ g/mol [56, 57, 59]. The fit to bitumen indicates a lower $S^2 \simeq 0.085$, implying a less-rigid molecule (i.e. more isotropic internal-motions). The second free-parameter is the local correlation-time τ_L , which characterizes the fast τ_L ($\simeq 10$'s ps) motions of the molecular branches. The fit indicates a local correlation time of $\tau_L \simeq 20$ ns for the polydisperse polymers, and a longer $\tau_L \simeq 53$ ns for bitumen. We note that unlike bitumen, the fit for the polydisperse polymers is not very sensitive to τ_L , therefore an upper bound $\tau_L \lesssim 20$ ns may be more appropriate for the polydisperse polymers.

	$\Delta\omega_R/2\pi$ (kHz)	R (Å)	S^2	τ_L (ps)	τ_0 (ns)
Bitumen	20	2.47	0.085	53	268
Polymer	20	1.85	0.147	20	42

TABLE II. Results of the fitting parameters to the model for polydisperse polymers and bitumen in the high viscosity regime. S^2 and τ_L are optimized from data in Fig. 8 using Eq. 10, while τ_0 is optimized from data in Fig. 9 using Eq. 11. $\Delta\omega_R$ and R are fixed.

Also shown in Fig. 8 are the MD simulations of the 1,000 cP polymer above $f_0 > 100$ MHz, corresponding viscosity independent region (see Fig. 6) where $T_1 \propto f_0$. The agreement between simulation and data/model in Fig. 8 is remarkable given that only a monodisperse model of poly(isobutene) is used in the simulations. This suggests that the $T_1 \propto f_0$ behavior is generic at high-viscosities, and that ^1H - ^1H dipole-dipole relaxation dominates over paramagnetism at high-viscosities.

B. T_{2LM} for polydisperse polymers and bitumen

The results for T_{2LM} for the crude oils are shown in Fig. 9(a), taken from various sources listed in the legend, with the most recent addition is the bitumen data at $f_0 = 400$ MHz by Kausik *et al.* [44]. T_{2LM} for the polydisperse polymers are shown in Fig. 7(b), along with de-oxygenated n -alkane data [41], and the MD simulation results for the polymers at 400 MHz.

Solid lines are fits using the model in Eq. 11 with fitting parameters shown in Table II, restricted to the high-viscosity region $\eta/T > 0.3$ cP/K, or $\eta > 100$ cP at ambient equivalently. Both the polydisperse polymers and bitumen data are consistent with $T_{2LM} \propto (\eta/T)^{-1/2}$ for viscosities higher than $\eta/T > 0.3$ cP/K. The model

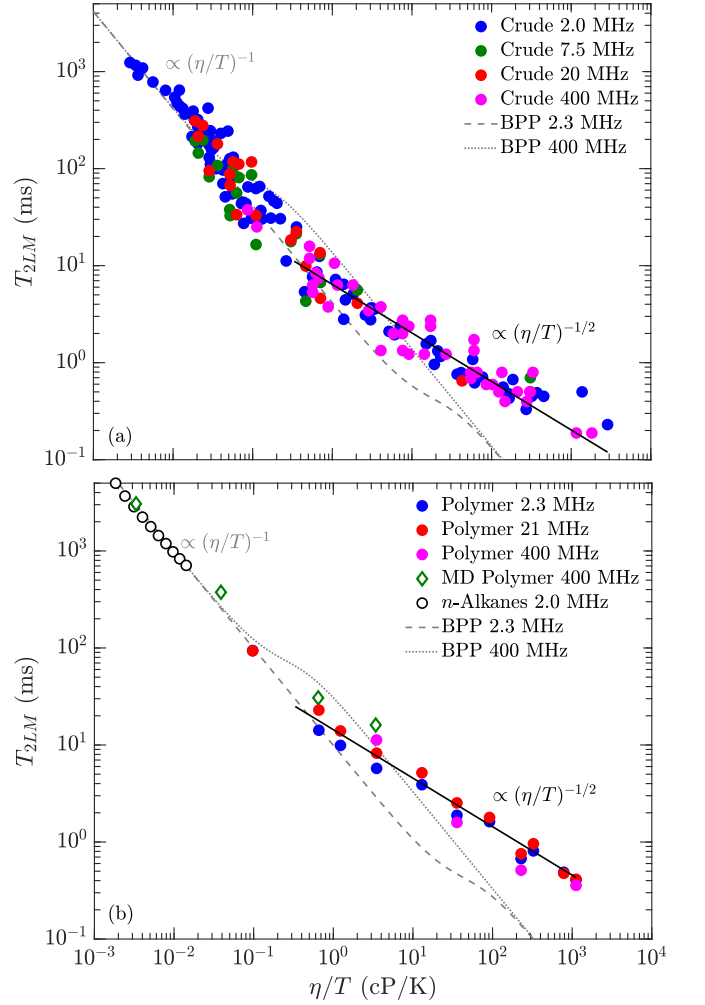


FIG. 9. (a) T_{2LM} vs. η/T for bitumen at 2.0 MHz (Vinegar *et al.* [2], LaTorraca *et al.* [6], Yang *et al.* [25]), at 7.5 MHz and 20 MHz (Zhang *et al.* [10]), and at 400 MHz (Kausik *et al.* [44]). (b) T_{2LM} vs. η/T for the polydispersed polymers in Table I at 2.3 MHz, 21 MHz, and 400 MHz, and MD simulations of the polymers at 400 MHz. n -Alkane de-oxygenated data at 2.0 MHz (Shikov *et al.* [41]). Solid lines are fits using the model in Eq. 11 for the region $\eta/T \gtrsim 0.3$ cP/K (or $\eta \gtrsim 100$ cP at ambient, equivalently), with fitting parameters listed in Table II. Curved lines are the BPP prediction [63] at 2.3 MHz and 400 MHz.

indicates that τ_0 is a factor $\simeq 6$ larger for bitumen than for the polydisperse polymers. As discussed in Section IIB 2, there are two explanations for $\tau_R = (\tau_\eta \tau_0)^{1/2} \propto (\eta/T)^{1/2}$ and the interpretation of constant τ_0 [37, 44], and more investigations are required to narrow down the theory.

The BPP model predicts a “kink” in T_2 during the transition from the low- to high-viscosity regimes, where T_2 is shifted up by a factor 10/3 with increasing viscosity. The kink is supposed to occur at a viscosity corresponding to $\omega_0 \tau_\eta = 0.615$, which as shown in Fig. 9 predicts an intermittent spread between low frequency

(2.3 MHz) and high frequency (400 MHz) data. However, no spread between the 2.3 MHz and 400 MHz T_{2LM} data is apparent (within uncertainties), for both polydisperse polymers and bitumen. In other words, there is no apparent frequency dependence in T_{2LM} (within uncertainties) during the low- to high-viscosity regime, at least up to 400 MHz. We also note that such a kink in T_{2LM} has never been reported before for polydisperse fluids with a broad T_2 distribution.

We also note that the MD simulations of the polymers agree well with the measurements, which again suggests that ^1H - ^1H dipole-dipole relaxation dominates over paramagnetism at high-viscosities.

C. Full frequency dependence of polydisperse polymer

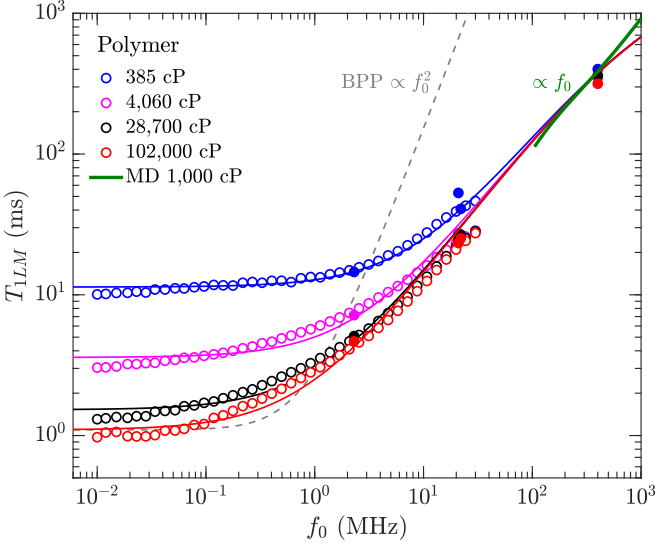


FIG. 10. T_{1LM} vs. f_0 from field-cycling (open symbols) and static fields (closed symbols) for the polydisperse polymers. Solid curves are results of the model in Eq. 8 with fixed values of S^2 and τ_L listed in Table II, along with optimized τ_0 listed in Table III. MD simulations of the 1,000 cP polymer are shown above $f_0 > 100$ MHz, corresponding to viscosity independent region (see Fig. 6) where $T_1 \propto f_0$. BPP prediction where $T_1 \propto f_0^2$ at high frequencies is also shown.

The full frequency dependence in T_{1LM} for the polydisperse polymer are presented in Fig. 10. Also shown are the fits from the full expression of the model in Eq. 8 using fixed values of S^2 and τ_L listed in Table II, and optimized values of τ_0 listed in Table III. The optimized values of τ_0 in Table III tend to decrease with increasing viscosity, however the average agrees with the value in Table II determined from the entire set of T_{2LM} data. The factor $\simeq 2$ smaller τ_0 (and factor $\simeq 2^{1/2}$ smaller τ_R) for 102,000 cP is likely due to FC ramp-time effects which overestimate T_{1LM} by a factor $\simeq 2^{1/2}$.

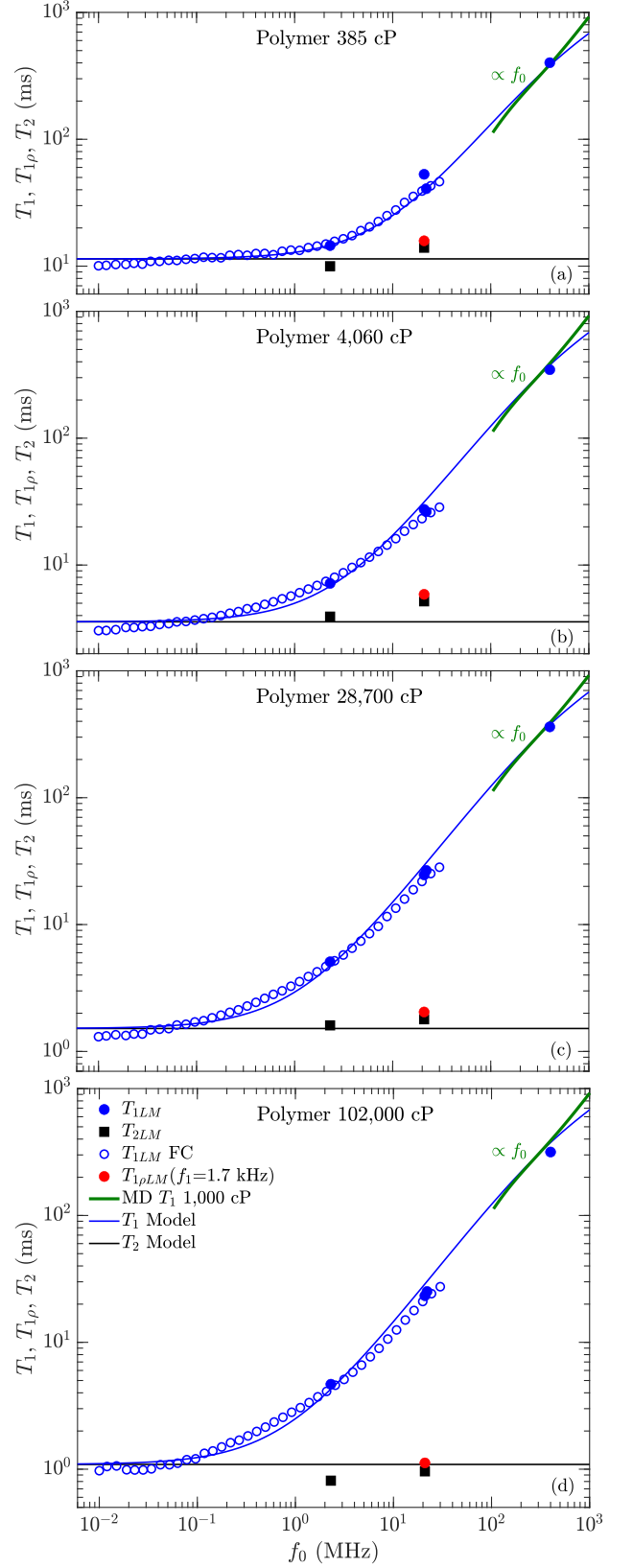


FIG. 11. T_{1LM} from Fig. 10, plus T_2 , $T_{1\rho}$, and model.

All at 40°C	η (cP)	τ_η (ns)	τ_0 (ns)	τ_R (ns)
	385	2	53	11
	4,060	25	51	36
	28,700	179	40	85
	102,000	636	22*	118*

TABLE III. Viscosity η , Stokes-Einstein-Debye correlation time τ_η (Eq. 3), τ_0 fitting parameter used in Fig. 10 and corresponding $\tau_R = (\tau_\eta \tau_0)^{1/2}$, for the polydisperse polymers at 40°C. (*) τ_0 and τ_R for 102,000 cP are likely underestimated due to FC ramp-time effects.

The full expression of the model shows good agreement with the data over the entire frequency range $f_0 = 0.01 \leftrightarrow 400$ MHz, including the coalescence at high frequencies corresponding to the slow-motion regime $\omega_0 \tau_R \gg 1$. Likewise, the MD simulation of the 1,000 cP polymer above $f_0 > 100$ MHz shows $T_1 \propto f_0$ behavior, consistent with the data and the model.

Fig. 11 shows the same T_{1LM} data as Fig. 10, along with T_{2LM} and $T_{1\rho LM}$ (at $f_1 = 1.7$ kHz) which show similar values to T_{1LM} at $f_0 = 0.01$ MHz. This implies that T_{2LM} and $T_{1\rho LM}$ ($f_1 = 1.7$ kHz) have no dependence on f_0 (within uncertainties), and remain in the fast-motion regime even when $\omega_0 \tau_R \gg 1$. We speculate this is due to the broad distribution in correlation times, which for T_1 is more efficiently narrowed by longitudinal cross-relaxation (a.k.a. spin-diffusion) than for T_2 by transverse cross-relaxation. This stems from the fact that transverse cross-relaxation for T_2 is only effective in the “non-secular” limit, i.e. the low frequency limit [76]. As such, we speculate that the transition from the fast-to slow-motion regime may occur over a much broader frequency range for T_2 than for T_1 . This is supported by the lack of frequency dependence (i.e. the lack of a kink) in T_{2LM} shown in Fig. 9(b). As such, we retain the factor 10/3 in Eq. 11 even in the slow-motion regime, at least up to 400 MHz.

IV. CONCLUSIONS

We present NMR relaxation measurements of polydisperse polymers over a wide range of viscosities and over a wide range of frequencies using T_1 and T_2 in static fields, T_1 field-cycling relaxometry, and $T_{1\rho}$ relaxation in the rotating frame.

We develop a phenomenological model to fit the relaxation data which accounts for a distribution in molecular correlation times for these polydisperse polymers by decreasing the frequency exponent in the BPP model [63] from $(\omega\tau)^2$ to $(\omega\tau)^1$ [42, 43]. Our model also accounts for internal motions of the non-rigid polymer branches with a Lipari-Szabo model incorporating an order parameter S^2 (i.e. rigidity), and a (fast) local correlation time τ_L

of the polymer branches. In the high viscosity regime of the model, the (slow) rotational correlation time of the entire polymer is taken to be $\tau_R = (\tau_\eta \tau_0)^{1/2} \propto (\eta/T)^{1/2}$, where $\tau_\eta \propto \eta/T$ is the Stokes-Einstein-Debye correlation time, and τ_0 is a constant interpreted in [37, 44].

In the high-viscosity (i.e. slow-motion) regime, the model accounts for the viscosity independent “plateau” $T_{1LM} \times 2.3/f_0 \simeq 3$ ms of the polydisperse polymers. The model accounts for previously reported bitumen data where the same plateau was reported, as well as the departure from the $T_{1LM} \propto f_0$ behavior at high frequencies $f_0 \gtrsim 100$ MHz. The model also accounts for the $T_{2LM} \propto (\eta/T)^{-1/2}$ behavior at high viscosities $\eta/T \gtrsim 0.3$ cP/K (or $\eta \gtrsim 100$ cP at ambient, equivalently), for both polydisperse polymers and bitumen.

The model is applied to the full range of frequencies f_0 covering both the fast- and slow-motion regimes of the polydisperse polymers. The data indicate that the T_{2LM} and $T_{1\rho}$ are independent of f_0 up to 400 MHz, which we speculate is because the transition from the fast-to slow-motion regime occurs over a much broader frequency range for T_2 than for T_1 . We speculate this may be a result of the broad distribution in correlation times together with cross-relaxation (a.k.a. spin-diffusion) effects.

Molecular dynamics simulations of T_1 and T_2 by ^1H - ^1H dipole-dipole relaxation of monodisperse polymers are reported with viscosities in the range $\eta = 1 \leftrightarrow 1,000$ cP. The simulations confirm the dominance of *intra*-molecular over *inter*-molecular ^1H - ^1H relaxation at high viscosity, which was previously only assumed to be the case. The simulations for $\eta \gtrsim 100$ cP show that $T_1 \propto f_0$ at high frequencies ($f_0 \gtrsim 100$ MHz), specifically $T_1 \times 2.3/f_0 \simeq 3$ ms, in good agreement with measurements and the model. A similar dispersion relation $T_{1S} \propto f_0$ was previously reported from MD simulations of the surface relaxation T_{1S} of heptane confined in a polymer matrix, specifically $T_{1S} \times 2.3/f_0 \simeq 7$ ms [53], implying a common NMR relaxation mechanism between high-viscosity fluids and low-viscosity fluids under confinement. The MD simulations also imply that ^1H - ^1H dipole-dipole relaxation dominates over paramagnetism for these systems.

SUPPORTING INFORMATION

1. Effects of dissolved oxygen.
2. Details of the new model.
3. Link between model and Cole-Davidson.
4. Details of the MD simulation.

ACKNOWLEDGMENTS

We thank the Chevron Corporation, the Rice University Consortium on Processes in Porous Media, and the American Chemical Society Petroleum Research Fund

(No. ACS PRF 58859-ND6) for funding this work. We gratefully acknowledge the National Energy Research Scientific Computing Center, which is supported by the Office of Science of the U.S. Department of Energy (No. DE-AC02-05CH11231) and the Texas Advanced Computing Center (TACC) at The University of Texas at

Austin for HPC time and support. We also thank Zeliang Chen, Maura Puerto, Lawrence B. Alemany, Kairan Zhu, Z. Harry Xie, Tuan D. Vo, Prof. Aydin Babakhani, Prof. Rafael Verduzco, Hao Mei, and Jinlu Liu for their contributions to Ref. [43], which paved the way for the further investigations reported here.

-
- [1] Zega, J. A.; House, W. V.; Kobayashi, R. A corresponding-states correlation of spin relaxation in normal alkanes *Physica A* **1989** 156 (1), 277–293
 - [2] Vinegar, H. J.; Tutunjian, P. N.; Edelstein, W. A.; Roemer, P. B. Whole-core analysis by ^{13}C NMR *Soc. Petrol. Eng. J.* **1991** 6 (2), 183–189
 - [3] Tutunjian, P. N.; Vinegar, H. J. Petrophysical applications of automated high-resolution proton NMR spectroscopy *Log Analyst* **1992** 136–144
 - [4] Morriss, C. E.; Freedman, R.; Straley, C.; Johnson, M.; Vinegar, H. J.; Tutunjian, P. N. Hydrocarbon saturation and viscosity estimation from NMR logging in the belridge diatomite *Log Analyst* **1997** 38 (2), 44–72
 - [5] Zhang, Q.; Lo, S.-W.; Huang, C. C.; Hirasaki, G. J.; Kobayashi, R.; House, W. V. Some exceptions to default NMR rock and fluid properties *Soc. Petrophys. Well Log Analysts* **1998** SPWLA-1998-FF
 - [6] LaTorraca, G. A.; Stonard, S. W.; Webber, P. R.; Carlson, R. M.; Dunn, K. J. Heavy oil viscosity determination using NMR logs *Soc. Petrophys. Well Log Analysts* **1999** SPWLA-1999-PPP
 - [7] Appel, M.; Freeman, J. J.; Perkins, R. B.; van Dijk, N. P. Reservoir fluid study by nuclear magnetic resonance *Soc. Petrophys. Well Log Analysts* **2000** SPWLA-2000-HH
 - [8] Freedman, R.; Lo, S.; Flaum, M.; Hirasaki, G. J.; Matteson, A.; Sezginer, A. A new NMR method of fluid characterization in reservoir rocks: Experimental confirmation and simulation results *Soc. Petrol. Eng. J.* **2001** 6 (4), 452–464
 - [9] Lo, S.-W.; Hirasaki, G. J.; House, W. V.; Kobayashi, R. Mixing rules and correlations of NMR relaxation time with viscosity, diffusivity, and gas/oil ratio of methane/hydrocarbon mixtures *Soc. Petrol. Eng. J.* **2002** 7 (1), 24–34
 - [10] Zhang, Y.; Hirasaki, G. J.; House, W. V.; Kobayashi, R. Oil and gas NMR properties: the light and heavy ends *Soc. Petrophys. Well Log Analysts* **2002** SPWLA-2002-HHH
 - [11] Bryan, J.; Mirotchnik, K.; Kantzas, A. Viscosity determination of heavy oil and bitumen using NMR relaxometry *J. Can. Petrol. Technol.* **2003** 42 (7), 29–34
 - [12] Freedman, R.; Heaton, N.; Flaum, M.; Hirasaki, G. J.; Flaum, C.; Hürlimann, M. Wettability, saturation, and viscosity from NMR measurements *Soc. Petrol. Eng. J.* **2003** 8 (4), 317–327
 - [13] Hirasaki, G. J.; Lo, S.-W.; Zhang, Y. NMR properties of petroleum reservoir fluids *Magn. Reson. Imaging* **2003** 21 (3-4), 269–277
 - [14] Chen, S.; Zhang, G.; Kwak, H.; Edwards, C. M.; Ren, J.; Chen, J. Laboratory investigation of NMR crude oils and mud filtrates properties in ambient and reservoir conditions *Soc. Petrol. Eng.* **2004** SPE-90553-MS
 - [15] Freedman, R.; Heaton, N. Fluid characterization using nuclear magnetic resonance logging *Petrophysics* **2004** 45 (3), 241–250
 - [16] Bryan, J.; Kantzas, A.; Bellehumeur, C. Oil-viscosity predictions from low-field NMR measurements *Soc. Petrol. Eng. J.* **2005** 8 (1), 44–52
 - [17] Winkler, M.; Freeman, J. J.; Appel, M. The limits of fluid property correlations used in NMR well logging: an experimental study of reservoir fluids at reservoir conditions *Petrophysics* **2005** 46 (2), 104–112
 - [18] Mutina, A. R.; Hürlimann, M. D. Effect of oxygen on the NMR relaxation properties of crude oils *Appl. Magn. Reson.* **2005** 29:503
 - [19] Nicot, B.; Fleury, M.; Leblond, J. A new methodology for better viscosity prediction using NMR relaxation *Soc. Petrophys. Well Log Analysts* **2006** SPWLA-2006-Z
 - [20] Straley, C. Reassessment of correlations between viscosity and NMR measurements *Soc. Petrophys. Well Log Analysts* **2006** SPWLA-2006-AA
 - [21] Freed, D. E. Dependence on chain length of NMR relaxation times in mixtures of alkanes *J. Chem. Phys.* **2007** 126, 174502
 - [22] Nicot, B.; Fleury, M.; Leblond, J. Improvement of viscosity prediction using NMR relaxation *Soc. Petrophys. Well Log Analysts* **2007** SPWLA-2007-U
 - [23] Burcaw, L.; Kleinberg, R.; Bryan, J.; Kantzas, A.; Cheng, Y.; Kharrat, A.; Badry, R. Improved methods for estimating the viscosity of heavy oils from magnetic resonance data *Soc. Petrophys. Well Log Analysts* **2008** SPWLA-2008-W
 - [24] Mutina, A. R.; Hürlimann, M. D. Correlation of transverse and rotational diffusion coefficient: a probe of chemical composition in hydrocarbon oils *J. Phys. Chem. A* **2008** 112, 3291–3301
 - [25] Yang, Z.; Hirasaki, G. J. NMR measurement of bitumen at different temperatures *J. Magn. Reson.* **2008** 192, 280–293
 - [26] Hürlimann, M. D.; Freed, D. E.; Zielinski, L. J.; Song, Y.-Q.; Leu, G.; Straley, C.; Minh, C. C.; Boyd, A. Hydrocarbon composition from NMR diffusion and relaxation data *Petrophysics* **2009** 50 (2), 116–129
 - [27] Lisitz, N. V.; Freed, D. E.; Sen, P. N.; Song, Y.-Q. Study of asphaltene nanoaggregation by nuclear magnetic resonance (NMR) *Energy Fuels* **2009** 23, 1189–1193
 - [28] Kantzas, A. Advances in magnetic resonance relaxometry for heavy oil and bitumen characterization *J. Can. Petrol. Technol.* **2009** 48 (3), 15–23
 - [29] Zielinski, L.; Saha, I.; Freed, D. E.; Hürlimann, M. D.; Liu, Y. Probing asphaltene aggregation in native crude oils with low-field NMR *Langmuir* **2010** 26(7), 5014–5021

- [30] Zielinski, L.; Hürlimann, M. D. Nuclear magnetic resonance dispersion of distributions as a probe of aggregation in crude oils *Energy Fuels* **2011** 25, 5090–5099
- [31] Yang, Z.; Hirasaki, G. J.; Appel, M.; Reed, D. A. Viscosity evaluation for NMR well logging of live heavy oils *Petrophysics* **2012** 53 (1), 22–37
- [32] Jones, M.; Taylor, S. E.; Keng, H. Two-dimensional magnetic resonance study of synthetic oil sands *Soc. Petrol. Eng.* **2014** SPE-170006-MS
- [33] Chen, J. J.; Hürlimann, M. D.; Paulsen, J.; Freed, D.; Mandal, S.; Song, Y.-Q. Dispersion of T_1 and T_2 nuclear magnetic resonance relaxation in crude oils *ChemPhysChem* **2014** 15, 2676–2681
- [34] Freedman, R.; Anand, V.; Grant, B.; Ganesan, K.; Tabrizi, P.; Torres, R.; Catina, D.; Ryan, D.; Borman, C.; Krueckl, C. A compact high-performance low-field NMR apparatus for measurements on fluids at very high pressures and temperatures *Rev. Sci. Instrum.* **2014** 85, 025102
- [35] Benamsili, L.; Korb, J.-P.; Hamon, G.; Louis-Joseph, A.; Bouyssiere, B.; Zhou, H.; Bryant, R. G. Multi-dimensional nuclear magnetic resonance characterizations of dynamics and saturations of brine/crude oil/mud filtrate mixtures confined in rocks: The role of asphaltene *Energy Fuels* **2014** 28, 1629–1640
- [36] Stapf, S.; Ordikhani-Seyedlar, A.; Ryan, N.; Mattea, C.; R.Kausik; Freed, D. E.; Song, Y.-Q.; Hürlimann, M. D. Probing maltene-asphaltene interaction in crude oil by means of NMR relaxation *Energy Fuels* **2014** 28, 2395–2401
- [37] Korb, J.-P.; Vorapalawut, N.; Nicot, B.; Bryant, R. G. Relation and correlation between NMR relaxation times, diffusion coefficients, and viscosity of heavy crude oils *J. Phys. Chem. C* **2015** 119 (43), 24439–24446
- [38] Vorapalawut, N.; Nicot, B.; Louis-Joseph, A.; Korb, J.-P. Probing dynamics and interaction of maltenes with asphaltene aggregates in crude oils by multiscale NMR *Energy Fuels* **2015** 29, 4911–4920
- [39] Jones, M.; Taylor, S. E. NMR relaxometry and diffusometry in characterizing structural, interfacial and colloidal properties of heavy oils and oil sands *Adv. Colloid Interface Sci.* **2015** 224, 33–45
- [40] Ordikhani-Seyedlar, A.; Neudert, O.; Stapf, S.; Mattea, C.; Kausik, R.; Freed, D. E.; Song, Y.-Q.; Hürlimann, M. D. Evidence of aromaticity-specific maltene NMR relaxation enhancement promoted by semi-immobilized radicals *Energy Fuels* **2016** 30, 3886–3893
- [41] Shikhov, I.; Arns, C. Temperature-dependent oxygen effect on NMR D - T_2 relaxation-diffusion correlation of n -alkanes *Appl. Magn. Reson.* **2016** 47 (12), 1391–1408
- [42] Singer, P. M.; Chen, Z.; Alemany, L. B.; Hirasaki, G. J.; Zhu, K.; Xie, Z. H.; Vo, T. D. NMR relaxation of polymer-alkane mixes, a model system for crude oils *Soc. Petrophysics. Well Log Analysts* **2017** SPWLA-2017-XX
- [43] Singer, P. M.; Chen, Z.; Alemany, L. B.; Hirasaki, G. J.; Zhu, K.; Xie, Z. H.; Vo, T. D. Interpretation of NMR relaxation in bitumen and organic shale using polymer-heptane mixes *Energy Fuels* **2018** 32 (2), 1534–1549
- [44] Kausik, R.; Freed, D.; Fellah, K.; Feng, L.; Ling, Y.; Simpson, G. Frequency and temperature dependence of 2D NMR T_1 - T_2 maps of shale *Petrophysics* **2019** 60 (1), 37–49
- [45] Markovic, S.; Bryan, J. L.; Turakhanov, A.; Cheremisin, A.; Mehta, S. A.; Kantzas, A. In-situ heavy oil viscosity prediction at high temperatures using low-field NMR relaxometry and nonlinear least squares *Fuel* **2020** 260, 116328
- [46] Washburn, K. E. Relaxation mechanisms and shales *Concepts Magn. Reson.* **2014** A 43 (3), 57–78
- [47] Singer, P. M.; Chen, Z.; Hirasaki, G. J. Fluid typing and pore size in organic shale using 2D NMR in saturated kerogen isolates *Petrophysics* **2016** 57 (6), 604–619
- [48] Fleury, M.; Romero-Sarmiento, M. Characterization of shales using T_1 - T_2 maps *J. Petrol. Sci. Eng.* **2016** 137, 55–62
- [49] Zhang, B.; Daigle, H. Nuclear magnetic resonance surface relaxation mechanisms of kerogen *Geophysics* **2017** 82(6), 15–22
- [50] Washburn, K. E.; Cheng, Y. Detection of intermolecular homonuclear dipolar coupling in organic rich shale by transverse relaxation exchange *J. Magn. Reson.* **2017** 278, 18–24
- [51] Tandon, S.; Heidari, Z. Improved analysis of NMR measurement in organic-rich mudrocks through quantifying hydrogen-kerogen interfacial relaxation mechanisms *Soc. Petrophysics. Well Log Analysts* **2019** SPWLA-2019-MMM
- [52] Xie, H.; Gan, Z. Investigation of physical properties of hydrocarbons in unconventional mudstones using two-dimensional NMR relaxometry *Soc. Petrophysics. Well Log Analysts* **2019** SPWLA-2019-ZZZ
- [53] Parambathu, A. V.; Singer, P. M.; Hirasaki, G. J.; Chapman, W. G.; Asthagiri, D. Molecular dynamics simulations of NMR relaxation and diffusion of heptane confined in a polymer matrix **2020** arXiv:2001.07310 <https://arxiv.org/abs/2001.07310>
- [54] Liu, J.; Chapman, W. G. Thermodynamic modeling of the equilibrium partitioning of hydrocarbons in nanoporous kerogen particles *Energy Fuels* **2019** 33 (2), 891–904
- [55] Abivin, P.; Taylor, S. D.; Freed, D. Thermal behavior and viscoelasticity of heavy oils *Energy Fuels* **2012** 26, 3448–3461
- [56] Kariyo, S.; Gainaru, C.; Schick, H.; Brodin, A.; Novikov, V. N.; Rössler, E. A. From a simple liquid to a polymer melt: NMR relaxometry study of polybutadiene *Physical Review Letters* **2006** 97, 207803
- [57] Kariyo, S.; Brodin, A.; Gainaru, C.; Herrmann, A.; Hintermeyer, J.; Schick, H.; Novikov, V. N.; Rössler, E. A. From simple liquid to polymer melt: glassy and polymer dynamics studied by fast field cycling NMR relaxometry: Rouse regime *Macromolecules* **2008** 41, 5322–5332
- [58] Kruk, D.; Herrmann, A.; Rössler, E. Field-cycling NMR relaxometry of viscous liquids and polymers *Prog. Nucl. Magn. Reson. Spect.* **2012** 63, 3364
- [59] Graf, R.; Heuer, A.; Spiess, H. W. Chain-order effects in polymer melts probed by ^1H double-quantum NMR spectroscopy *Physical Review Letters* **1998** 80 (26), 5738–5741
- [60] Chávez, F. V.; Saalwächter, K. Time-domain NMR observation of entangled polymer dynamics: Universal behavior of flexible homopolymers and applicability of the tube model *Macromolecules* **2011** 44, 1549–1559
- [61] Chávez, F. V.; Saalwächter, K. Time-domain NMR observation of entangled polymer dynamics: Analytical theory of signal functions *Macromolecules* **2011** 44,

- 1560–1569
- [62] Mordvinkin, A.; Saalwächter, K. Microscopic observation of the segmental orientation autocorrelation function for entangled and constrained polymer chains *J. Chem. Phys.* **2017** 146, 094902
- [63] Bloembergen, N.; Purcell, E. M.; Pound, R. V. Relaxation effects in nuclear magnetic resonance absorption *Phys. Rev.* **1948** 73 (7), 679–712
- [64] Davidson, D. W.; Cole, R. H. Dielectric relaxation in glycerol, propylene glycol, and *n*-propanol *J. Chem. Phys.* **1951** 19, 1484
- [65] Lindsey, C. P.; Patterson, G. D. Detailed comparison of the WilliamsWatts and ColeDavidson functions *J. Chem. Phys.* **1980** 73, 3348
- [66] Flämig, M.; Hofmann, M.; Fatkullin, N.; Rössler, E. A. NMR relaxometry: The canonical case glycerol *J. Phys. Chem. B* **2020** 124, 1557–1570
- [67] Lipari, G.; Szabo, A. Model-free approach to the interpretation of nuclear magnetic resonance relaxation in macromolecules. 1. Theory and range of validity *J. Amer. Chem. Soc.* **1982** 104, 4546–4559
- [68] Lipari, G.; Szabo, A. Model-free approach to the interpretation of nuclear magnetic resonance relaxation in macromolecules. 2. Analysis of experimental results *J. Amer. Chem. Soc.* **1982** 104, 4559–4570
- [69] Holden, G. Viscosity of polyisoprene *J. Appl. Polym. Sci.* **1965** 9, 2911–2925
- [70] Zhao, B.; Shaw, J. M. Composition and size distribution of coherent nanostructures in Athabasca bitumen and Maya crude oil *Energy Fuels* **2007** 21, 2795–2804
- [71] Kimmich, R. *NMR Tomography, Diffusometry and Relaxometry* Springer-Verlag **1997**
- [72] Steiner, E.; Yemloul, M.; Guendouz, L.; Leclerc, S.; Robert, A.; Canet, D. NMR relaxometry: Spin lattice relaxation times in the laboratory frame versus spin lattice relaxation times in the rotating frame *Chem. Phys. Lett.* **2010** 495, 287–291
- [73] Venkataramanan, L.; Song, Y.-Q.; Hürlimann, M. D. Solving fredholm integrals of the first kind with tensor product structure in 2 and 2.5 dimensions *IEEE Trans. Sig. Process.* **2002** 50 (5), 1017–1026
- [74] Song, Y.-Q.; Venkataramanan, L.; Hürlimann, M. D.; Flaum, M.; Frulla, P.; Straley, C. T_1 - T_2 correlation spectra obtained using fast two-dimensional laplace inversion *J. Magn. Reson.* **2002** 154, 261–268
- [75] Kalk, A.; Berendsen, H. J. C. Proton magnetic relaxation and spin diffusion in proteins *J. Magn. Reson.* **1976** 24, 343–366
- [76] Kowalewski, J.; Mäler, L. *Nuclear Spin Relaxation in Liquids: Theory, Experiments, and Applications* Taylor & Francis Group **2006**
- [77] Kimmich, R.; Ansaldo, E. Field-cycling NMR relaxometry *Prog. Nucl. Magn. Reson. Spect.* **2004** 44, 257–320
- [78] Roos, M.; Hofmann, M.; Link, S.; Ott, M.; Balbach, J.; Rössler, E.; Saalwächter, K.; Krushelnitsky, A. The “long tail” of the protein tumbling correlation function: observation by ^1H NMR relaxometry in a wide frequency and concentration range *J. Biomol. NMR* **2015** 63, 403415
- [79] Ward-Williams, J.; Korb, J.-P.; Gladden, L. F. Insights into functionality-specific adsorption dynamics and stable reaction intermediates using fast field cycling NMR *J. Phys. Chem. C* **2018** 122, 20271–20278
- [80] McConnell, J. *The Theory of Nuclear Magnetic Relaxation in Liquids* Cambridge University Press **1987**
- [81] Cowan, B. *Nuclear Magnetic Resonance and Relaxation* Cambridge University Press **1997**
- [82] Woessner, D. E. Spin relaxation processes in a two-proton system undergoing anisotropic reorientation *J. Chem. Phys.* **1962** 36 (1), 1–4
- [83] Woessner, D. E. Nuclear magnetic dipole-dipole relaxation in molecules with internal motion *J. Chem. Phys.* **1965** 42 (6), 1855–1859
- [84] Orazio, F. D.; Bhattacharj, S.; Halperin, W. P.; Eguchi, K.; Mizusaki, T. Molecular diffusion and nuclear-magnetic-resonance relaxation of water in unsaturated porous silica glass *Physical Review B* **1990** 42, 9810
- [85] Torrey, H. C. Nuclear spin relaxation by translational diffusion *Phys. Rev.* **1953** 92 (4), 962–969
- [86] Hwang, L.-P.; Freed, J. H. Dynamic effects of pair correlation functions on spin relaxation by translational diffusion in liquids *J. Chem. Phys.* **1975** 63 (9), 4017–4025
- [87] Singer, P. M.; Asthagiri, D.; Chapman, W. G.; Hirasaki, G. J. Molecular dynamics simulations of NMR relaxation and diffusion of bulk hydrocarbons and water *J. Magn. Reson.* **2017** 277, 15–24
- [88] Asthagiri, D.; Singer, P. M.; Parambathu, A. V.; Chen, Z.; Hirasaki, G. J.; Chapman, W. G. Molecular dynamics simulations of NMR relaxation and diffusion of bulk hydrocarbons *SEG/AAPG/EAGE/SPE Research and Development Petroleum Conference and Exhibition* **2018** 101–102
- [89] Singer, P. M.; Asthagiri, D.; Chen, Z.; Valiya Parambathu, A.; Hirasaki, G. J.; Chapman, W. G. Role of internal motions and molecular geometry on the NMR relaxation of hydrocarbons *J. Chem. Phys.* **2018** 148 (16), 164507
- [90] Teng, C.-L.; Hong, H.; Kiihne, S.; Bryant, R. G. Molecular oxygen spinlattice relaxation in solutions measured by proton magnetic relaxation dispersion *J. Magn. Reson.* **2001** 148, 31–34
- [91] Lauffer, R. B. Paramagnetic metal complexes as water proton relaxation agents for NMR imaging: Theory and design *Chem. Rev.* **1987** 87, 901–927
- [92] Abragam, A. *Principles of Nuclear Magnetism* Oxford University Press, International Series of Monographs on Physics **1961**
- [93] Singer, P. M.; Asthagiri, D.; Chapman, W. G.; Hirasaki, G. J. NMR spin-rotation relaxation and diffusion of methane *J. Chem. Phys.* **2018** 148 (20), 204504
- [94] Abramowitz, M.; Stegun, I. A. *Handbook of Mathematical Functions with Formulas, Graphs, and Mathematical Tables* chapter 5: Exponential integral and related functions Dover Publications (1983) edition **1964**
- [95] Magin, R. L.; Li, W.; Velasco, M. P.; Trujillo, J.; Reiter, D. A.; Morgenstern, A.; Spencer, R. G. Anomalous NMR relaxation in cartilage matrix components and native cartilage: Fractional-order models *J. Magn. Reson.* **2010** 210, 184–191
- [96] Beckmann, P. A. Spectral densities and nuclear spin relaxation in solids *Phys. Rep.* **1988** 171 (3), 85–128
- [97] Phillips, J. C.; Braun, R.; Wang, W.; Gumbart, J.; Tajkhorshid, E.; Villa, E.; Chipot, C.; Skeel, R. D.; Kale, L.; Schulten, K. Scalable molecular dynamics with NAMD *J. Comput. Chem.* **2005** 26(16), 1781–1802
- [98] Theoretical and Computational Biophysics group, NIH Center for Macromolecular Modeling and

- Bioinformatics, at the Beckman Institute, University of Illinois at Urbana-Champaign NAMD **2018**
<http://www.ks.uiuc.edu/Research/namd/>
- [99] Vanommeslaeghe, K.; Hatcher, E.; Acharya, C.; Kundu, S.; Zhong, S.; Shim, J.; Darian, E.; Guvench, O.; Lopes, P.; Vorobyov, I.; Jr., A. D. M. CHARMM general force field: A force field for drug-like molecules compatible with the CHARMM all-atom additive biological force field *J. Comput. Chem.* **2010** 31, 671–690
- [100] ParamChem CGenFF 3.0.1
<https://cgenff.paramchem.org> **2020**
- [101] Bakhmutov, V. I. *NMR Spectroscopy in Liquids and Solids* CRC Press, Taylor & Francis Group **2015**

V. SUPPORTING INFORMATION

A. Effects of dissolved oxygen

The measured $T_{1,2}$ of a bulk fluid at atmospheric conditions are given by the following:

$$\frac{1}{T_{1,2}} = \frac{1}{T_{1B,2B}} + \frac{1}{T_{1O_2,2O_2}} \quad (13)$$

$T_{1B,2B}$ are the bulk contributions from ^1H - ^1H dipole-dipole relaxation. For de-oxygenated n -alkanes at ambient it was previously shown that $T_{1B,2B} = 9.56 (\eta/T)^{-1}$ [9], which for n -heptane is $T_{1B,2B} = 7,320$ ms at 25°C (where $\eta = 0.39$ cP).

Given the measured $T_{1,2}$ and the known $T_{1B,2B}$ for n -heptane at ambient, Eq. 13 yields the paramagnetic contribution T_{1O_2} from dissolved oxygen. As shown in Fig. 12(a), T_{1O_2} increases from $T_{1O_2} = 2,500$ ms at $f_0 = 2.3$ MHz to $T_{1O_2} = 5,600$ ms at $f_0 = 400$ MHz. T_{1O_2} depends on the electron correlation time τ_e and the concentration C_{O_2} of dissolved oxygen through the following relations [80]:

$$\frac{1}{T_{1O_2}} = J_{O_2}(\omega_0) + \frac{7}{3}J_{O_2}(\omega_e), \quad (14)$$

$$\frac{1}{T_{2O_2}} = \frac{2}{3}J_{O_2}(0) + \frac{1}{2}J_{O_2}(\omega_0) + \frac{13}{6}J_{O_2}(\omega_e), \quad (15)$$

where the BPP spectral density is given by:

$$J_{O_2}(\omega) = \frac{1}{3}\Delta\omega_{O_2}^2 \frac{2\tau_e}{1 + (\omega\tau_e)^2} \text{ with } \Delta\omega_{O_2}^2 \propto C_{O_2} \quad (16)$$

τ_e is the electron correlation time of the paramagnetic O_2 molecule, and the second moment (i.e. strength) is given by $\Delta\omega_{O_2}^2 \propto C_{O_2}$. Note that the Larmor frequency of the electron ω_e is larger than ^1H by a factor $\omega_e \simeq 659\omega_0$. The BPP model for the spectral density $J_{O_2}(\omega)$ was previously shown to work well for a variety of solvents of various molecular weights [90]. Fig. 12(a) shows that the fit to T_{1O_2} using Eqs. 14 and 16 work well, with best fit parameters $\tau_e = 1.15$ ps (which is consistent with [90]) and $\Delta\omega_{O_2}/2\pi = 62.8$ kHz.

Given that the concentration of dissolved oxygen in n -heptane is $C_{O_2} = 132$ mg/L (or 4.12 mM equivalently) at ambient ($p_{O_2} = 0.21$ atm) implies that the relaxivity (defined in MRI terminology [91]) of O_2 is $r_1 = 0.10$ $\text{mM}^{-1}\text{s}^{-1}$ at low frequencies $f_0 \lesssim 100$ MHz.

As shown in [90], τ_e is roughly constant for solvents with the molecular weight of heptane or higher, and also appears roughly constant at lower molecular weights [79]. Furthermore as shown in Fig. 12(b), MD simulations indicate that C_{O_2} is $\sim 30\%$ less for the 1,000 cP polymer than for heptane [53], implying that T_{1O_2} is $\sim 30\%$ larger for the polymer than for heptane. This predicts that $T_{1O_2} \simeq 8,000$ ms for the polymer at $f_0 = 400$ MHz, which is much larger than the measured $T_1 \simeq 300$ ms. In other words, the effects of oxygen on $T_{1,2}$ are negligible

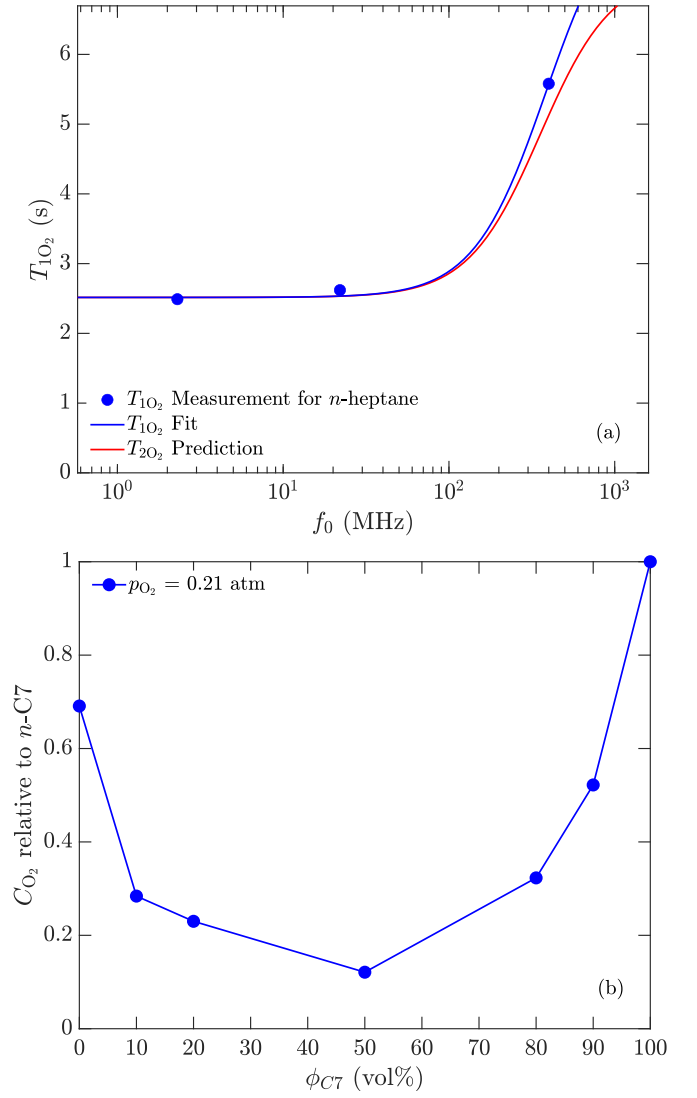


FIG. 12. (a) Measurement of paramagnetic relaxation time T_{1O_2} due to dissolved oxygen in n -heptane [43] determined from Eq. 13, along with fit using Eq. 14. Prediction for T_{2O_2} also shown. (b) MD simulation of concentration C_{O_2} of dissolved oxygen in 1,000 cP polymer ($\phi_{C7} = 0$ vol%) relative to n -heptane ($\phi_{C7} = 100$ vol%) under ambient conditions, along with simulations for various polymer-heptane mixes, taken from [53].

for the polymer at 400 MHz. Below 400 MHz, the effects of oxygen on the polymer are even less since the measured $T_{1,2} \ll 300$ ms.

The only cases in this report where the effects of dissolved oxygen are apparent are for the low-viscosity crude-oils at $f_0 \lesssim 100$ MHz where $T_{1LM,2LM} \gtrsim 1,000$ ms. In such cases $T_{1LM,2LM}$ deviate slightly from the BPP correlation line $T_{1LM,2LM} = 4.0 (\eta/T)^{-1}$ in the low-viscosity regime.

B. Details of the model

The autocorrelation function $G(t)$ for fluctuating magnetic ^1H - ^1H dipole-dipole interactions is central to the development of the NMR relaxation theory in liquids [63, 71, 80, 81, 85, 86, 92]. From $G(t)$, one can determine the spectral density function $J(\omega)$ by Fourier transform as such:

$$J(\omega) = 2 \int_0^\infty G(t) \cos(\omega t) dt, \quad (17)$$

for $G(t)$ in units of s^{-2} [80]. As shown in Fig. 13(a), $G(t)$ for the n -alkanes has a multi-exponential (i.e. “stretched”) decay rather than the single exponential decay predicted by BPP. Furthermore, the degree of stretching increases with increasing carbon number (i.e. increasingly non-spherical geometry). MD simulations indeed confirm that n -pentane and n -hexane have a more stretched intra-molecular $G_R(t)$ autocorrelation function (i.e. a broader distribution of correlation times) than the symmetric neo-pentane and benzene molecules, respectively [89]. The degree of stretching can be further analyzed using inverse Laplace transforms (see also [93] and supporting information in [89]).

By comparison, Fig 13(b) shows the effect of decreasing the exponent β in the spectral density function $J^{(\beta)}(\omega)$ as such:

$$J^{(\beta)}(\omega) = \frac{1}{3} \Delta\omega_R^2 \frac{2\tau}{1 + (\omega\tau)^{2\beta}}, \quad (18)$$

$$G^{(\beta)}(t) = \frac{2}{2\pi} \int_0^\infty J^{(\beta)}(\omega) \cos(\omega t) d\omega, \quad (19)$$

where the real part of the inverse Fourier transform $G^{(\beta)}(t)$ is also defined. An analytical expression for $G^{(\beta)}(t)$ exists for the two extreme cases:

$$\frac{G^{(1)}(t)}{G^{(1)}(0)} = \exp(-t/\tau), \quad (20)$$

$$\frac{G^{(1/2)}(t)}{G^{(1/2)}(0)} = \frac{2}{\pi} \int_0^\infty \frac{\cos(x)}{x + t/\tau} dx. \quad (21)$$

The case of $\beta = 1$, $G^{(1)}(t)$, is the BPP model with a single-exponential decay. The case of $\beta = 1/2$, $G^{(1/2)}(t)$ [94], is the stretched case used in the phenomenological model to account for the independence of T_{1LM} on τ , i.e. the independence on η/T . As demonstrated in Fig 13, increasing the carbon number increases the degree of stretching in Fig 13(a), which corresponds to decreasing β in Fig 13(b).

It is interesting to note that the long time behavior of Eq. 21 is $G^{(1/2)}(t) \propto t^{-2}$ for $t/\tau \gg 10$. This is analogous to the Mittag-Leffler function, which starts off as a stretched exponential at short times, and turns into a power-law decay at long times [95].

We note that $G^{(1/2)}(t)$ starts to diverge below $t/\tau = 0.14$, therefore the model is valid for times $t/\tau \gtrsim 0.14$.

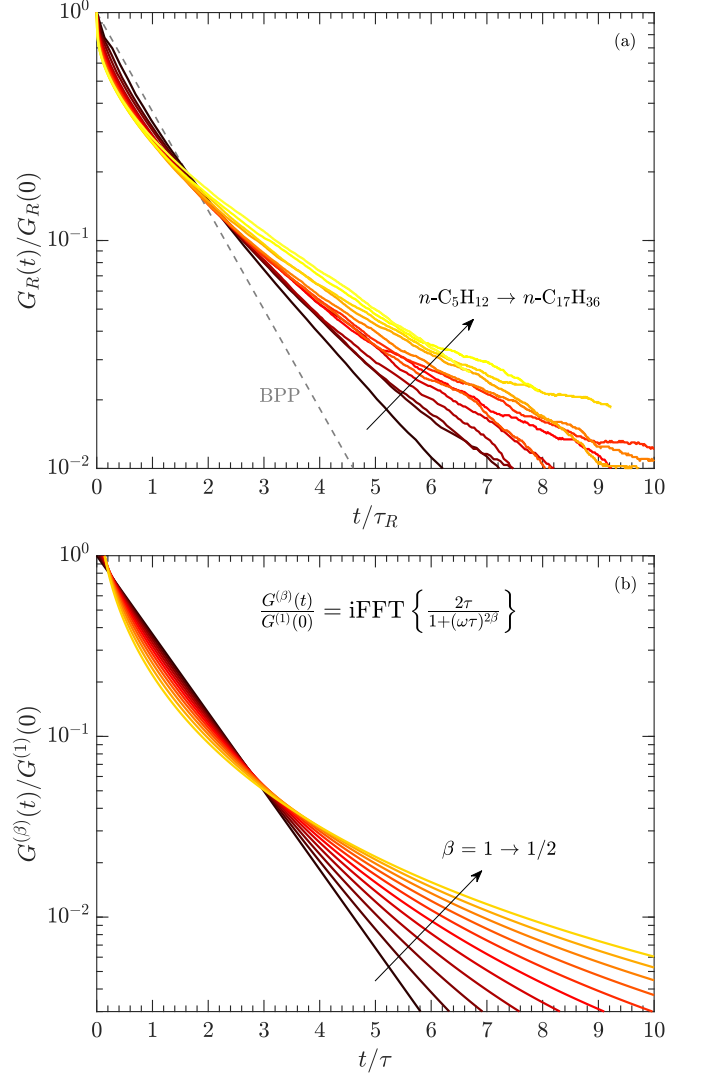


FIG. 13. (a) MD simulations of the intra-molecular autocorrelation function $G_R(t)$ for the liquid n -alkanes at ambient, taken from [87]. The y -axis is normalized by the zero time amplitude $G_R(0)$, and the x -axis is normalized by the correlation time τ_R . Straight line is the BPP prediction. (b) Inverse Fourier transform $G^{(\beta)}(t)$ (Eq. 19) of the spectral density function $J^{(\beta)}(\omega)$ (Eq. 18), where $\beta = 1$ corresponds to BPP model (Eq. 20), and $\beta = 1/2$ (Eq. 21) corresponds to the model in this report.

Correspondingly, this implies that the model for $J^{(1/2)}(\omega)$ is valid for frequencies $2\omega\tau \lesssim 7.1$ (where the factor 2 reflects the $J(2\omega_0)$ terms in Eq. 1). Given the local correlation-time $\tau_L \simeq 50$ ps, this corresponds to validity below frequencies $f_0 \lesssim 10$ GHz.

C. Link between model and Cole-Davidson

The Cole-Davidson function is widely used to describe the dielectric response [64, 65, 96] and its departure from the traditional Debye model. The function is defined as such:

$$\chi''(\omega) = \text{Im} \left\{ \left(\frac{1}{1 + i\omega\tau_{CD}} \right)^{\beta_{CD}} \right\} \quad (22)$$

which reduces to the following expression:

$$\chi''(\omega) = \frac{\sin[\beta_{CD} \arctan(\omega\tau_{CD})]}{[1 + (\omega\tau_{CD})^2]^{\beta_{CD}/2}}. \quad (23)$$

The Cole-Davidson exponent is bound by $0 < \beta_{CD} \leq 1$, where $\beta_{CD} = 1$ is the Debye model. As β_{CD} is decreased, the underlying distribution $P_{CD}(\tau)$ in molecular correlation times τ grows wider.

The Cole-Davidson function has also been successfully used to describe NMR relaxation of glycerol and monodispersed polymers through the relation $\chi''_{DD}(\omega) \propto \omega/T_1$ [58, 66]. The NMR Cole-Davidson spectral density $J_{CD}(\omega)$ is given by the following:

$$J_{CD}(\omega) = \frac{2}{\omega} \text{Im} \left\{ \left(\frac{1}{1 + i\omega\tau_{CD}} \right)^{\beta_{CD}} \right\} \frac{\frac{1}{3}\Delta\omega_R^2}{\beta_{CD}\pi/2} \quad (24)$$

which reduces to the following expression:

$$J_{CD}(\omega) = \frac{2}{\omega} \frac{\sin[\beta_{CD} \arctan(\omega\tau_{CD})]}{[1 + (\omega\tau_{CD})^2]^{\beta_{CD}/2}} \frac{\frac{1}{3}\Delta\omega_R^2}{\beta_{CD}\pi/2}. \quad (25)$$

For the purposes of comparison with our model, we have added a factor $\frac{1}{3}\Delta\omega_R^2/\beta_{CD}\pi/2$ to the definition of $J_{CD}(\omega)$. The factor $\frac{1}{3}\Delta\omega_R^2$ is related to the units convention of the spectral density [81]. The factor $1/\beta_{CD}\pi/2$ is introduced to highlight the similarity with our model. $J_{CD}(\omega)$ as defined in Eq. 25 becomes independent of β_{CD} in the limit $\beta_{CD} \lesssim 10^{-3}$, and tends towards:

$$J_{CD}(\omega) \Rightarrow \frac{1}{3}\Delta\omega_R^2 \frac{2\tau_R}{1 + \omega\tau_R} \quad \text{for} \quad \begin{cases} \beta_{CD} \lesssim 10^{-3} \\ \tau_{CD} = \tau_R \pi/2 \end{cases} \quad (26)$$

In other words, $J_{CD}(\omega)$ tends towards our model (without the added Lipari-Szabo model, i.e. $S^2 = 1$) in the case of $\beta_{CD} \lesssim 10^{-3}$ and $\tau_{CD} = \tau_R \pi/2$. Fig 14 shows T_1 determined from $J_{CD}(\omega)$ for $\beta_{CD} = 1, 0.6$, and 10^{-3} , compared with our model. The similarity between $J_{CD}(\omega)$ for $\beta_{CD} \lesssim 10^{-3}$ and our model is remarkable, and only shows a $\simeq 22\%$ deviation at the transition from the fast- to slow-motion regime. The deviation for T_2 (not shown) $\simeq 14\%$ is even less.

Fig 14 also indicates the corresponding cases as BPP ($\beta_{CD} = 1$), glycerol ($\beta_{CD} \simeq 0.6$ for the α -peak [58, 64, 66]), and our model for polydisperse polymers and bitumen ($\beta_{CD} \lesssim 10^{-3}$). Also shown are the limiting behavior

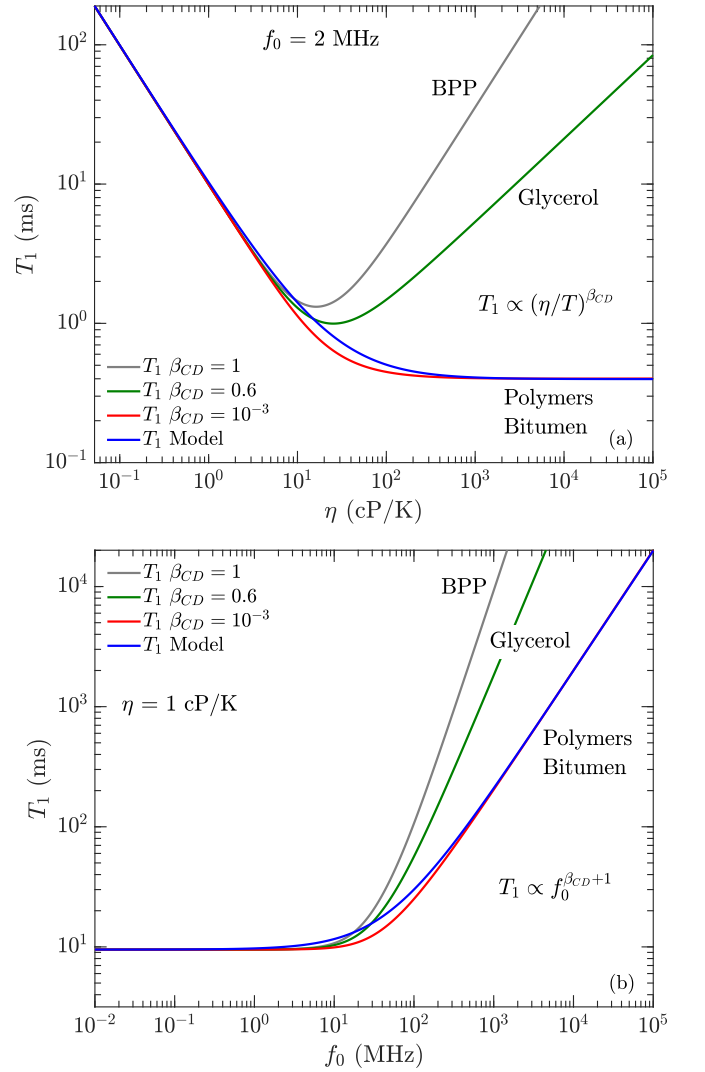


FIG. 14. T_1 determined from $J_{CD}(\omega)$ for $\beta_{CD} = 1, 0.6$, and 10^{-3} , compared with our model, (a) as a function of η/T for fixed $f_0 = 2$ MHz, and (b) as a function of f_0 for fixed $\eta/T = 1$ cP/K.

in according to Cole-Davidson in the slow-motion regime $T_1 \propto f_0^{\beta_{CD}+1} (\eta/T)^{\beta_{CD}}$.

The above comparison shows that polydisperse polymers and bitumen have a much larger distribution in molecular correlation times than glycerol. In terms of the Cole-Davidson model, this manifests itself as a small exponent $\beta_{CD} \lesssim 10^{-3}$ for the polydisperse polymers and bitumen, compared to monodisperse glycerol where $\beta_{CD} \simeq 0.6$ for the α -peak.

D. Details of MD simulation

The detailed simulation procedure is provided in Ref. [53]. The system was simulated using NAMD [97, 98] code, and modeled using CGenFF Force Field[99, 100]. The number of molecules used were 269, 143, 74, and 40 for the 2-mer, 4-mer, 8-mer and 16-mer, respectively. The systems were equilibrated at constant NpT conditions at 25°C and 1 atm. The data was then collected in a NVE ensemble to compute the autocorrelations $G_{R,T}(t)$.

The results of the intra-molecular $G_R(t)$ and inter-molecular $G_T(t)$ are shown in Fig. 15(a) for the polymer at 1 cP and 1,000 cP. In order to quantify the departure of $G_{R,T}(t)$ from single-exponential decay, we fit $G_{R,T}(t)$ to a sum of multi-exponential decays and determine the underlying probability distribution $P_{R,T}(\tau)$ in correlation times τ . More specifically, we perform an inversion of the following Laplace transform [73, 74, 89]:

$$G_{R,T}(t) = \int_0^\infty P_{R,T}(\tau) \exp(-t/\tau) d\tau, \quad (27)$$

$$\tau_{R,T} = \frac{1}{G_{R,T}(0)} \int_0^\infty P_{R,T}(\tau) \tau d\tau, \quad (28)$$

$$G_{R,T}(0) = \frac{1}{3} \Delta\omega_{R,T}^2 \quad (29)$$

where $P_{R,T}(\tau)$ are the probability distribution functions derived from the inversion, plotted in Fig. 15(b). Details of the inversion procedure can be found in [93] and in the supporting information in [89].

The $P_{R,T}(\tau)$ in Fig. 15(b) indicate a set of ~ 5 polymer modes, located at similar τ values for both intra-molecular $P_R(\tau)$ and inter-molecular $P_T(\tau)$ interactions. The intra-molecular $P_R(\tau)$ has an additional mode at short $\tau \sim 10^{-2}$ ps for both the polymer and heptane, while it is absent for $P_T(\tau)$ in both cases. Similar observation of the $\tau \sim 10^{-2}$ ps mode was reported in the supporting information for all the liquid-state n -alkanes [89], and it is attributed to the fast rotation of the methyl groups.

The decomposition of $G_{R,T}(t)$ into a sum of exponential decays is common practice in phenomenological models of complex molecules [96, 101], where the more complex the molecular dynamics, the more exponential terms are required [82, 83]. This is in contrast to analytical techniques and theories used to interpret the auto-correlation function of monodisperse polymers with high molecular-weight $M_w > 4,000$ g/mol where entanglement occurs, and a power law decay is observed $G(t) \propto t^{-\alpha}$ [60–62]. We note however that our polydisperse polymers most likely do not entangle to the extent that monodisperse polymers do, if indeed the polydisperse polymers entangle at all.

Also defined in Eq. 28 are the correlation times $\tau_{R,T}$ derived from $P_{R,T}(\tau)$, which are found to be $\tau_R = 2,380$ ps and $\tau_T = 3,030$ ps at 1,000 cP, compared with $\tau_R = 3.33$ ps and $\tau_T = 10.1$ ps at 1 cP. In other words, the MD simulations indicate that $\tau_{R,T}$ increase by a factor

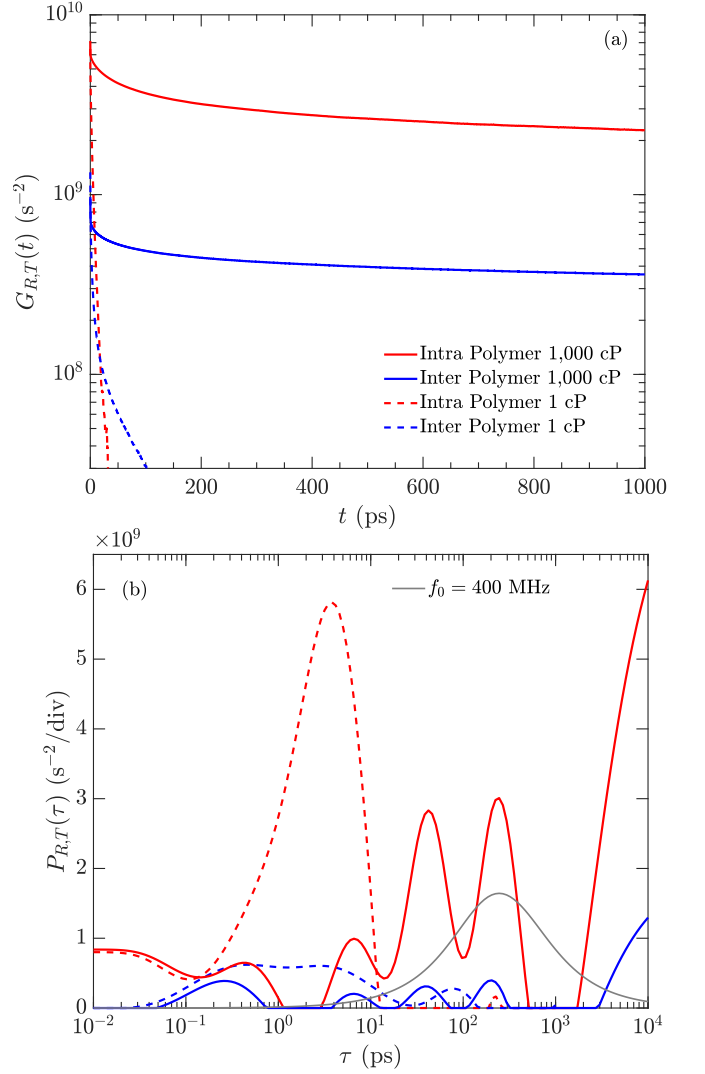


FIG. 15. (a) MD simulations of the intra-molecular ($G_R(t)$) and inter-molecular ($G_T(t)$) auto-correlation functions $G_{R,T}(t)$ for polymer at 1,000 cP and 1 cP. (b) Probability distributions $P_{R,T}(\tau)$ determined from inverse Laplace transforms of $G_{R,T}(t)$ (Eq. 27). Gray curve is BPP frequency filter defined in Eq. 30, at $f_0 = 400$ MHz.

of $\simeq 500$ from 1 cP to 1,000 cP.

The spectral density $J_{R,T}(\omega)$ is determined from the Fourier transform (Eq. 17) of $G_{R,T}(t)$ (Eq. 27):

$$J_{R,T}(\omega) = \int_0^\infty \frac{2\tau}{1 + (\omega\tau)^2} P_{R,T}(\tau) d\tau \quad (30)$$

from which the $T_{1,2}$ dispersion (i.e. frequency depen-

dence) can be determined as such:

$$\frac{1}{T_{1,R,T}} = J_{R,T}(\omega_0) + 4J_{R,T}(2\omega_0), \quad (31)$$

$$\frac{1}{T_{2,R,T}} = \frac{3}{2}J_{R,T}(0) + \frac{5}{2}J_{R,T}(\omega_0) + J_{R,T}(2\omega_0), \quad (32)$$

$$\frac{1}{T_{1,2}} = \frac{1}{T_{1R,2R}} + \frac{1}{T_{1T,2T}}. \quad (33)$$

Fig. 15(a) indicates that the second moment $\Delta\omega_{R,T}^2 = 3 G_{R,T}(0)$ is about a factor $\simeq 10$ larger for intra-molecular ($\Delta\omega_R^2$) versus inter-molecular ($\Delta\omega_R^2$) interactions at 1,000 cP. Given that $\tau_R \simeq \tau_T$ at 1,000 cP, one can then deduce that the ratio $T_{1T,2T}/T_{1R,2R} \simeq 10$. In other words, the intra-molecular relaxation rate is $\simeq 10$ larger than the inter-molecular relaxation rate, therefore intra-molecular relaxation dominates at 1,000 cP.

The gray curve in Fig. 15(b) corresponds to the “BPP frequency filter” defined in Eq. 30, at $f_0 = 400$ MHz (as an example). In other words, the components of $P_{R,T}(\tau)$ contributing to T_1 at $f_0 = 400$ MHz are weighted by the BPP frequency filter curve, which peaks at $\omega_0\tau = 0.615$. As such, the components in $P_{R,T}(\tau)$ at long $\tau \simeq 10^4$ ps do not contribute to T_1 at $f_0 = 400$ MHz (as an example), nor do the short components $\tau \lesssim 10$ ps.